ELSEVIER

A consistent approach for the coupling of radiation and hydrodynamics at low Mach number

Bruno Dubroca [a], Mohammed Seaïd [b], Ioan Teleaga [c,*]

[a] *MAB, UMR 5466, LRC M03, Université Bordeaux I, 315 cours de la libération, 33400 Talence, France*
[b] *Fachbereich Mathematik, Technische Universität Kaiserslautern, D-67663 Kaiserslautern, Germany*
[c] *Fachbereich Mathematik, Technische Universität Darmstadt, D-64289 Darmstadt, Germany*

Abstract

We present a consistent numerical model for coupling radiation to hydrodynamics at low Mach number. The hydrodynamical model is based on a low-Mach asymptotic in the compressible flow that removes acoustic wave propagation while retaining the compressibility effects resulting from combustion. Radiative transfer is modelled by the M_1 entropy equations that can be viewed as a moment method. The radiation model possesses the capability to accurately approximate solution of radiative transfer at low computational cost while retaining the main physical properties of radiative energy. Consistent numerical approaches are developed for space and time discretizations in both hydrodynamics and radiation. A modified projection method is used for hydrodynamics, whereas an HLL-type discretization is implemented for radiation transport. The combined methods permit time steps that are controlled by the advective time scales resulting in a substantial improvement in computational efficiency compared to a compressible formulation. Numerical results are presented for the natural convection in a squared cavity with large temperature difference and also for a diffusion methane/air flame with four-step reduced chemical reactions in non-gray participating media. The present approach has been found to be feasible and satisfactory.
© 2007 Elsevier Inc. All rights reserved.

Keywords: Radiation hydrodymanics; Low-Mach number flows; M_1 model; Natural convection; Diffusion flame

1. Introduction

Simultaneously occurring flow, combustion, convection and radiation in enclosures occur in several practical phenomena such as nuclear reactor safety, combustion, furnaces, fires and flames among others. In many of these applications, the characteristic flow velocity is very small and the characteristic temperature difference in the enclosure is very large. The first property requires modelling of low Mach number flows for

---

* Corresponding author. Tel.: +49 0 1791210405.
E-mail addresses: Bruno.Dubroca@math.u-bordeaux1.fr (B. Dubroca), seaid@mathematik.uni-kl.de (M. Seaïd), teleaga@mathematik.tu-darmstadt.de (I. Teleaga).

which compressible solvers are inappropriate, while the second property allows large density and temperature gradients which cannot be modelled by the canonical Boussinesq approximation of incompressible flows. On the other hand, it is common for studies on heat transfer to neglect other modes of heat transport such as thermal radiation. This mainly because, the modelling of radiative transfer involves complex mathematics, high computational cost, lack of chemical kinetics database, and significant uncertainty concerning the optical properties of the participating media and surfaces. However, radiation can strongly interact with convection in many situations of engineering interest, compare for example [13,16] and further discussions can be found therein. For instance, the influence of radiation on natural convection is generally stronger than that on forced convection due to the inherent coupling between the temperature and flow fields in enclosures. Therefore, our goal in this paper is to develop a consistent approach for radiating and reacting flows at low Mach number that are not only realistic enough to yield meaningful calculations, but also simple and fast enough to avoid overcharging the computational cost. This goal is reached by combining a low Mach asymptotic in the flow equations with an entropy moment model for the radiative transfer equation.

Our interest is in the development of a fast and accurate algorithm which is capable of solving reacting flows at low Mach number in radiating media ranging from optically thick to optically thin regimes. There are several reasons that justify the development of such algorithm. The first and the most important is that in many situations, such as methane/air flame, low Mach number coexists in the flow domain with radiative transfer in the participating gas where different optical and time scales may occur. Another more practical motivation is that an algorithm that can successfully solve flow at low Mach number coupled with radiative transfer in optically thin media using consistent space and time discretizations is well suited for abroad range of applications typically handled with incompressible formulations for flow and Monte Carlo method for radiation. Indeed, for low Mach numbers, the compressible Navier–Stokes equations describe almost incompressible flow. This singular limit of compressible flow equations is reasonably well understood such that, under some assumptions on the flow and some regularity conditions on the initial and boundary data, the solution of compressible equations, in the zero Mach number limit, can be shown to satisfy the incompressible flow equations [17]. From the computational point of view, accurate solutions of low Mach flows are difficult to obtain. This is due to the very different magnitude of the wave speeds which are present in the system. To overcome these difficulties, we consider the low Mach asymptotic reported in [17] and also used by the authors in [7,33] for modelling fire events in vehicular tunnels. The key idea consists of expanding the flow variables in powers of the Mach number leading to incompressible flow which allows density variations. This results in significant computational savings, since the time step is limited only by the convective velocity and not by the acoustic velocity. It should be stressed that the emphasis in the current work is on the development of approximate models for radiative transfer coupled to reacting flows at low Mach numbers. Therefore, the radiative models presented in this paper can be incorporated into other existing models for low Mach flows, for example those studied in [21] where turbulent effects are also accounted for in the low Mach number model and the discrete-ordinates method is used for the radiative transfer.

In the full simulation of combustion systems, the radiative transfer, which is an integro-differential equation, must be solved along with the partial differential equations of material, momentum, energy transport and chemical reactions as a fully coupled system. The most accurate procedures available in the literature for computing radiative transfer are the zonal and Monte Carlo methods [19]. However, these methods are not widely applied in comprehensive combustion calculations due to their large computational time and storage requirements. Also, the equations of radiative transfer are in non-differential form, a significant inconvenience when solved in conjunction with the differential equations of flow and combustion. Most of the current work on modeling energy transport in high-temperature gases or chemically reacting flows uses CFD codes. Therefore, the models for solving the radiative transfer must be compatible with the numerical methods employed to solve the reacting flow equations. The zonal and Monte Carlo methods for solving the radiative transfer problem are incompatible with the mathematical formulations used in CFD codes, and require prohibitive computational times for the spatial resolution desired. The S_n discrete-ordinate methods [5] appear to be reasonable compromises for solving the radiative transfer equations, but still one has to deal with large systems of algebraic equations, resulting from discretizing angle and space coordinates, that may deteriorate the efficiency of the CFD code.

Approximate models for radiative transfer have also been derived and widely used in the literature. As example for such approximations we cite the diffusion (Rosseland) approach and the simplified P_N equations, see [6,12,33] among others. These simplified models are derived by asymptotic analysis and perform very well when the medium under consideration is isotropic and optically thick (opaque). In fact, in an opaque medium the system is close to a radiative equilibrium for which assumptions of diffusion and simplified P_N equations are satisfied. However, for anisotropic or transparent (optically thin) media, the system is far from the radiative equilibrium and the previous approximate equations are no longer valid, see [29] for a situation where the P_N models produce nonphysical solutions. Another way to derive approximate equations for the radiative transfer is by taking suitable moments and closure relations, we refer the reader to [1–4,14] for more details on the moment approximations. In the current work, the entropy M_1 moment is selected to describe the radiative signal in reacting flows at low Mach number. The M_1 model is closed by a maximum entropy closure which introduces good properties in the model such as flux limited by the speed of light and dissipation of the local entropy. Furthermore, the M_1 model is a hyperbolic system of partial differential equations that can be solved by already existing numerical tools from CFD codes.

The focus in the present work is on combined convection and radiation in gas or gas mixture where accurate modelling of radiative transfer is required. Therefore, numerical results and applications are presented for three test problems with different orders of difficulty. First, we verify the validity of the moment model for a purely radiative transfer equation by comparing its accuracy and efficiency to a direct solver for the kinetic radiative transfer equation. In the second example we solve the buoyancy flow in a squared cavity with vertical side wall differentially heated with large temperature difference. Our method accurately resolves this natural convection-radiation problem. The last example considers a diffusion methane/air flame involving a reduced four-step chemical reactions for reacting species in non-gray gas. Our findings have shown that radiation heat loss can affect not only the flame temperature but also the velocity field and the concentrations of chemical species such as CO_2 and HO_2. Furthermore, in the considered flame, radiation can be an important energy loss mechanism affecting the flame structure, and radiative heat transfer can be commonly the most significant mode of energy transfer in industrial-scale combustion systems.

The organization of this paper is as follows. In Section 2 we formulate the mathematical models for chemically reacting flow and radiative transfer. We briefly discuss the low-Mach asymptotic for the fluid dynamics, the simplified chemical mechanism for reacting flow, and the entropy M_1 model for radiation transfer. In Section 3 we describe the solution procedure for the governing equations. Section 4 is devoted to numerical results for different test examples. We present results for natural convection in a squared cavity with large temperature difference and also for a diffusion methane/air flame in rectangular enclosure. Conclusions are summarized in Section 5.

2. Equations of low-Mach number reacting flow

The governing equations for unsteady compressible flow are the full Navier–Stokes equations describing conservation of mass, momentum, energy and species in a viscous Newtonian fluid. A dimensionless form of the equations is retained. In dimensional form, these equations are

$$
\begin{aligned}
&\partial_t \rho^* + \nabla \cdot (\rho^* \mathbf{u}^*) = 0, \\
&\partial_t \mathbf{u}^* + (\mathbf{u}^* \cdot \nabla)\mathbf{u}^* + \frac{1}{\rho^*}\nabla p^* = \frac{\mu}{\rho^*}\left(\Delta \mathbf{u}^* + \frac{1}{3}\nabla(\nabla \cdot \mathbf{u}^*)\right) + \mathbf{g}^*, \\
&\partial_t (c_v \rho^* T^*) + \nabla \cdot (c_v \mathbf{u}^* \rho^* T^*) + p^* \nabla \cdot \mathbf{u}^* = \nabla \cdot (K \nabla T^*) - \nabla \cdot q_R^* + \sum_{i=1}^{N_s} \dot{w}_i^*, \\
&\partial_t (\rho^* Y_i^*) + \nabla \cdot (\mathbf{u}^* \rho^* Y_i^*) = -\nabla \cdot (\rho^* Y_i^* V_i) + \dot{w}_i^*, \quad i = 1, \ldots, N_s,
\end{aligned}
\tag{2.1}
$$

where $\rho^*(t, \mathbf{x})$, $\mathbf{u}^*(t, \mathbf{x})$, $p^*(t, \mathbf{x})$, $T^*(t, \mathbf{x})$ and $Y_i^*(t, \mathbf{x})$ denote, respectively, the mass density, the flow velocity, the thermal pressure, the fluid temperature and the mass fraction of the ith species. Here, V_i is the diffusion velocity of the ith species, defined for example in [39]. The terms $\mathbf{g}^*$ and q_R^* describe the gravitational force and radiative heat flux, respectively. The quantities μ, K, c_v are the dynamic viscosity, the heat conductivity

and the specific heat coefficient at constant volume, respectively, whereas D_{ij} which appears in the definition of V_i is the binary coefficient of species i and j with N_s is the total number of reacting species. The nondimensional form of the system (2.1) is obtained by scaling every variable by its characteristic values as follows:

$$\mathbf{x} = \frac{\mathbf{x}^*}{x_{\text{ref}}}, \quad t = \frac{t^*}{t_{\text{ref}}}, \quad \sigma = \frac{\sigma^*}{\sigma_{\text{ref}}}, \quad K = \frac{K^*}{K_{\text{ref}}}, \quad Y_i = \frac{Y_i^*}{Y_{\text{ref}}},$$
$$\rho = \frac{\rho^*}{\rho_{\text{ref}}}, \quad \mathbf{u} = \frac{\mathbf{u}^*}{u_{\text{ref}}}, \quad T = \frac{T^*}{T_{\text{ref}}}, \quad p = \frac{p^*}{p_{\text{ref}}}, \quad I = \frac{I^*}{I_{\text{ref}}}, \tag{2.2}$$

where the subscript $_{\text{ref}}$ and superscript * represent reference and dimensional quantities, respectively. In (2.2), x_{ref}, t_{ref}, σ_{ref}, K_{ref}, Y_{ref}, ρ_{ref}, u_{ref}, T_{ref}, p_{ref} and I_{ref} denote a characteristic length, time, absorption, thermal conductivity, mass fraction, density, velocity, temperature, pressure and radiative intensity, respectively. Canonical dimensionless numbers are defined by

$$\tau = \sigma_{\text{ref}} x_{\text{ref}}, \quad \gamma = \frac{c_p}{c_v}, \quad M^2 = \frac{\rho_{\text{ref}} u_{\text{ref}}^2}{\gamma p_{\text{ref}}}, \quad Re = \frac{\rho_{\text{ref}} u_{\text{ref}} x_{\text{ref}}}{\mu}, \quad Pr = \frac{\mu c_p}{K},$$
$$Sc = \frac{\mu}{\rho_{\text{ref}} x_{\text{ref}}}, \quad Da = \frac{t_{\text{ref}} W_O A_0}{\rho_{\text{ref}}}, \quad Fr = \frac{u_{\text{ref}}}{\sqrt{x_{\text{ref}} \|\mathbf{g}\|}}, \quad \mathbf{g} = \frac{\mathbf{g}^*}{Fr^2 \|\mathbf{g}^*\|}. \tag{2.3}$$

Here τ, γ, M, Re, Pr, Fr, Sc, Da are the optical thickness, the adiabatic exponent, the Mach number, the Reynolds number, the Prandtl number, the Froude number, the Schmidt number, and the pre-exponential Damköhler number, respectively. The coefficients c_v and c_p are the specific heat coefficients at constant volume and pressure, respectively. In the definition of the pre-exponential Damköhler number, W_O and A_0 represent, respectively, the molecular weight of the oxygen species and the characteristic reaction rate, see for instance [20] for more details. Hence, the fluid dynamics system we consider in this paper reads

$$\partial_t \rho + \nabla \cdot (\rho \mathbf{u}) = 0,$$
$$\partial_t \mathbf{u} + \mathbf{u} \cdot \nabla \mathbf{u} + \frac{1}{\gamma M^2} \frac{1}{\rho} \nabla p = \frac{1}{Re} \frac{1}{\rho} \left(\nabla^2 \mathbf{u} + \frac{1}{3} \nabla (\nabla \cdot \mathbf{u}) \right) + \mathbf{g},$$
$$\partial_t (\rho T) + \nabla \cdot (\mathbf{u} \rho T) + (\gamma - 1) p \nabla \cdot \mathbf{u} = \frac{\gamma}{Pr} \frac{1}{Re} \nabla^2 T - \tau \int_0^\infty \int_{\mathbb{S}^2} \sigma (B(T, v) - I) \, d\Omega \, dv + \sum_{i=1}^{N_s} \dot{w}_i,$$
$$\partial_t (\rho Y_i) + \nabla \cdot (\mathbf{u} \rho Y_i) = \frac{1}{Re \, Sc} \nabla^2 Y_i + Da \dot{w}_i, \quad i = 1, \ldots, N_s, \tag{2.4}$$

where $I(t, v, \Omega, \mathbf{x})$ denotes the radiative intensity. We have used $\mathbb{S}^2$ to denote the unit sphere, $\mathbf{x}$ the space coordinate, t the time variable, Ω the directional angle and v the frequency variable. The fluid dynamic model is closed by the equation of state for an ideal gas,

$$p = R \rho T \sum_{i=1}^{N_s} \frac{Y_i}{W_i}, \tag{2.5}$$

where $R = c_p - c_v$ and W_i is the molecular weight of species i. The spectral intensity $I(t, v, \Omega, \mathbf{x})$ at time t, in position $\mathbf{x}$, within frequency v and propagating along direction Ω with a speed c, is obtained from the non-scattering radiative transfer equation

$$\frac{1}{c} \partial_t I + \tau \Omega \cdot \nabla I + \sigma I = \sigma B(T, v), \tag{2.6}$$

where $\sigma(v)$ is the absorption coefficient and $B(T, v)$ is the spectral intensity of the black-body radiation given by the Planck function

$$B(T, v) = \frac{2 h_P v^3}{c^2} \frac{1}{\exp\left(\frac{h_P v}{k_B T}\right) - 1}, \tag{2.7}$$

with h_P, k_B and c are Planck constant, Boltzmann constant and the speed of radiation propagation in the medium, respectively. For more details on physical aspects and mathematical equations for radiation hydrodynamics we refer to [18,19,22] and further references are cited therein. Eqs. (2.4)–(2.6) have to be solved in a bounded spatial domain $\mathscr{D}$ with smooth boundary $\partial\mathscr{D}$, equipped with given boundary and initial conditions. These conditions are problem dependent and their discussion is postponed for Section 4 where numerical examples are presented.

Note that chemically reacting flows require in addition to (2.4) and (2.6) a set of equations for reaction rates. A simplified chemical mechanism of four-step reactions for diffusion methane/air flames is formulated in Section 2.2.

2.1. Low Mach approximation for hydrodynamic flow

An important class of practical applications in reacting flows occur at low Mach numbers which lead to a fast characteristic time-scale associated with the propagation of acoustic waves. In this case, the wave velocity is equal to maximum of the flow speed and the velocity of sound. It is well known that using the compressible equations (2.4) for low-Mach numbers is inefficient. A way to overcome this drawback is to perform an asymptotic analysis with respect to the Mach number, see [17] for more details.

The derivation of the low-Mach number equations is obtained by expanding the pressure, temperature and velocity variables in terms of the scale $\epsilon = \gamma M^2$

$$p = p^{(0)} + \epsilon p^{(1)} + \dots, \tag{2.8}$$

with a similar equation for the temperature T and velocity $\mathbf{u}$. The variables $p^{(0)}$ and $p^{(1)}$ can be interpreted as a thermodynamic pressure and a fluid dynamic pressure, respectively. Introducing the expansion into Eq. (2.4) and balancing all terms of the same power of ϵ, the asymptotic equations of leading, first and second order are obtained [7,33]. Omitting the details here, the asymptotic analysis can be summarized as follows. From the leading order of the pressure equation, the time dependency of the pressure $p^{(0)}$ is given by

$$\partial_t p^{(0)} + \gamma p^{(0)} \nabla \cdot \mathbf{u} = \frac{\gamma p^{(0)}}{Pr\,Re} \nabla^2 \left(\frac{1}{\rho}\right) + q, \tag{2.9}$$

where q represents the sum of the radiation and chemical sources, see (2.4). In the relation below, $\mathbf{u}$ and ρ are zero order terms.

As in [7,33], we used that the gradient of the thermodynamic pressure is constant in space. Hence, by integrating Eq. (2.9) over the computational domain $\mathscr{D}$ and applying the Gauss theorem we obtain

$$|\mathscr{D}|\partial_t p^{(0)} + \frac{\gamma p^{(0)}}{|\mathscr{D}|} \int_{\partial\mathscr{D}} \mathbf{u} \cdot \mathbf{n} \, ds = \frac{\gamma p^{(0)}}{Pr\,Re} \int_{\mathscr{D}} \left(\nabla \frac{1}{\rho}\right) \cdot \mathbf{n} \, dx + \int_{\mathscr{D}} q \, dx, \tag{2.10}$$

where $|\mathscr{D}|$ and $\mathbf{n}$ denotes the area of $\mathscr{D}$ and the unit outward normal vector on the boundary $\partial\mathscr{D}$, respectively. An initial condition for (2.10) is

$$p^{(0)} = 1. \tag{2.11}$$

The system (2.10) and (2.11) represents a first order initial value problem for $p^{(0)}$. Because our numerical scheme (see Section 3) has first order accuracy, by considering the integral terms in (2.10) constant in time, a solution to (2.10) and (2.11) is

$$p^{(0)}(t) = \exp(-At) + \frac{C}{A}, \tag{2.12}$$

where

$$A = \frac{\gamma}{|\mathscr{D}|} \int_{\partial\mathscr{D}} \mathbf{u} \cdot \mathbf{n} \, ds - \frac{\gamma}{|\mathscr{D}|Pr\,Re} \int_{\partial\mathscr{D}} \left(\nabla \frac{1}{\rho}\right) \cdot \mathbf{n} \, ds, \quad C = \frac{1}{|\mathscr{D}|} \int_{\mathscr{D}} q \, dx.$$

Then, by inserting (2.10) and (2.12) into (2.9) yields

$$\nabla \cdot \mathbf{u} = \frac{1}{\gamma} A + \frac{1}{Pr\,Re} \Delta \frac{1}{\rho} + \frac{q - C}{\gamma \left(\exp(-At) + \frac{C}{A} \right)}. \tag{2.13}$$

For more details on the procedure below, we refer to [32]. Hence, in leading order Eqs. (2.4) reduce to

$$\partial_t \rho + \nabla \cdot (\rho \mathbf{u}) = 0,$$

$$\partial_t \mathbf{u} + (\mathbf{u} \cdot \nabla)\mathbf{u} + \frac{1}{\rho}\nabla p = \frac{1}{Re}\frac{1}{\rho}\left(\nabla^2 \mathbf{u} + \frac{1}{3}\nabla(\nabla \cdot \mathbf{u})\right) + \mathbf{g},$$

$$\nabla \cdot \mathbf{u} = Q, \tag{2.14}$$

$$\partial_t Y_i + \nabla \cdot (Y_i \mathbf{u}) = \frac{1}{Re\,Sc}\nabla^2 Y_i + \dot{w}_i, \quad i = 1, \dots, N_s,$$

with $p = p^{(1)}$ is hydrodynamic pressure and Q is the right-hand side term of (2.13). The fluid temperature T in leading order is deduced from the density as

$$T = \frac{p^{(0)}}{\rho}. \tag{2.15}$$

Using the modified projection method described in [7], the nonlinear system (2.14) can be expressed as

$$\partial_t \rho + \nabla \cdot (\rho \mathbf{u}) = 0,$$

$$\partial_t \mathbf{u} + (\mathbf{u} \cdot \nabla)\mathbf{u} + \frac{1}{\rho}\nabla p = \frac{1}{Re}\frac{1}{\rho}\left(\nabla^2 \mathbf{u} + \frac{1}{3}\nabla Q\right) + \mathbf{g},$$

$$\nabla \cdot \left(\frac{1}{\rho}\nabla p\right) = \nabla \cdot \left(\frac{1}{Re}\frac{1}{\rho}\left(\nabla^2 \mathbf{u} + \frac{1}{3}\nabla Q\right) + \mathbf{g}\right), \tag{2.16}$$

$$\partial_t Y_i + \nabla \cdot (Y_i \mathbf{u}) = \frac{1}{Re\,Sc}\nabla^2 Y_i + Da\dot{w}_i, \quad i = 1, \dots, N_s.$$

Another early approach to derive low-Mach number equations was presented in [21]. By differentiating the equation of state (2.5) with respect to time variable, the authors in [21] obtained a different version of the velocity-divergence constraint. The resulting system was then used to simulate unsteady, non-premixed reacting flows. In addition, it is clear that the low Mach equations used by the authors in [7,33] for non-reacting flows can be retained if open systems are considered or no compression from the outside takes place. In these situations, collecting the zeroth order terms in the momentum equation yields to a thermodynamic pressure $p^{(0)}$ which is constant in space and can only be a function of time. Moreover, because the radiation does not appears explicitly in the momentum equation, it does not affect the pressure $p^{(0)}$ in space, it will affect its time-dependence, see (2.9).

Note that, when the Mach number $M \geqslant 1$ the whole asymptotic approach is not valid anymore and the pressure $p^{(0)}$ cannot be constant in space. Furthermore, assuming that the domain has an open entry or exit, $\partial_t p^{(0)}$ in (2.9) can be neglected resulting a non-constant velocity divergence. A rigorous mathematical justification of such asymptotic analysis can be found in [11].

2.2. Simplified four-step model for chemical reactions

In general, the set of N_r elementary reversible chemical reactions involving N_s chemical species S_i can be represented in compact form as follows

$$\sum_{i=1}^{N_s} v_{ij}^f S_i \rightleftharpoons \sum_{i=1}^{N_s} v_{ij}^b S_i, \quad j = 1, 2, \dots, N_r, \tag{2.17}$$

where v_{ij}^f and v_{ij}^b are the ith species stoichiometric constants for the jth forward and backward reaction, respectively. The net rate of creation of species i by chemical reaction is given by

$$\dot{\omega}_i = \dot{\omega}_i^+ - \dot{\omega}_i^-, \tag{2.18}$$

with $\dot{\omega}_i^+$ and $\dot{\omega}_i^-$ are the production and destruction rates of species i given by

$$\dot{\omega}_i^+ = W_i \sum_{j=1}^{N_r} \left(v_{ij}^b R_j^f + v_{ij}^f R_j^b \right), \quad \dot{\omega}_i^- = W_i \sum_{j=1}^{N_r} \left(v_{ij}^f R_j^f + v_{ij}^b R_j^b \right), \tag{2.19}$$

where W_i is the molecular weight of the ith species. The forward and the backward reaction rates are defined as
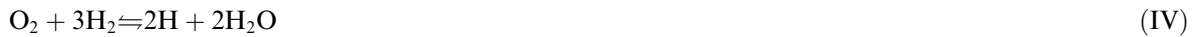
$$R_j^f = \left(\sum_{i=1}^{N_s} \alpha_{ij} C_i \right) k_j^f \prod_{i=1}^{N_s} C_i^{v_{ij}^f}, \quad R_j^b = \left(\sum_{i=1}^{N_s} \alpha_{ij} C_i \right) k_j^b \prod_{i=1}^{N_s} C_i^{v_{ij}^b}. \tag{2.20}$$

Here, α_{ij} is the third body efficiency for the ith species in the jth reaction, $C_i = \rho Y_i / W_i$ is the molar concentration of the ith species. The forward and backward reaction rate constants by the modified Arrhenius law are given by

$$k_j^f = A_j^f T^{\beta_j} \exp\left(-\frac{E_j^f}{RT} \right), \quad k_j^b = \frac{k_j^f}{K_j^c}, \tag{2.21}$$

where A_j, β_j, E_j^f and K_j^c are the pre-exponential factor, temperature exponent, activation energy and equilibrium constant, respectively.

The chemical kinetic mechanisms for gas flames are described in detail in various available literatures, see [39,37,31] among others. We therefore restrain ourselves to brief summary and further details can be found in the above mentioned references. In the current work we use a reduced chemical model based on a four-step chemical mechanism proposed in [31] for methane/air flames. The model consists of the following chemical reactions:

$$CH_4 + 2H + H_2O \rightarrow CO + 4H_2 \tag{I}$$

$$CO + H_2O \rightleftharpoons CO_2 + H_2 \tag{II}$$

$$H + H + M \rightarrow H_2 + M \tag{III}$$

$$O_2 + 3H_2 \rightleftharpoons 2H + 2H_2O \tag{IV}$$

The associated reaction rates are defined as

$$\begin{aligned}
\dot{\omega}_I &= k_{11} C_{CH_4} C_H, \\
\dot{\omega}_{II} &= k_{10} \frac{C_H}{C_{H_2}} \left(C_{CO} C_{H_2O} - \frac{C_{CO_2} C_{H_2}}{K_{II}} \right), \\
\dot{\omega}_{III} &= k_5 C_{O_2} C_H C_M, \\
\dot{\omega}_{IV} &= k_1 C_H \left(C_{O_2} - \frac{C_H^2 C_{H_2O}^2}{K_{IV} C_{H_2}^3} \right),
\end{aligned} \tag{2.22}$$

where the equilibrium constants are given by

$$K_{II} = 3.828 \times 10^{-5} T^{0.8139} e^{9839/RT}, \quad K_{IV} = 11.283 T^{-0.2484} e^{11400/RT}.$$

The values of reaction-rate constants appearing in (2.22) are listed in Table 1. The concentration of the third body C_M is calculated from the catalytic efficiency of species and its molecular weight as

Table 1
Reaction-rate constants

Reaction rate	$\hat{A}_i$	β_i	E_i
k_1	1.2×10^{17}	-0.91	69.10
k_5	2.0×10^{18}	-0.8	0.0
k_{10}	1.656×10^7	1.5247	60.042
k_{11}	2.2×10^4	3.0	36.6

Units in cm, mol, Kelvin and kJ.

$$C_{\mathrm{M}} = \sum_{i=1}^{N_s} \eta_i C_i,$$

with catalytic efficiencies $\eta_{\mathrm{CH_4}} = \eta_{\mathrm{H_2O}} = 6.5$, $\eta_{\mathrm{O_2}} = \eta_{\mathrm{N_2}} = 0.4$, $\eta_{\mathrm{CO_2}} = 1.5$, $\eta_{\mathrm{CO}} = 0.75$ and $\eta_{\mathrm{H_2}} = \eta_{\mathrm{H}} = 1$, compare [27]. With the reduced reaction mechanism only seven conservation equations for the species C_4, CO_2, CO, O_2, H_2O, H_2, and H are required to be solved. The inert species, N_2, is recovered from these seven species. The reaction rates $\dot{\omega}_i$ for the source terms in equations (2.16) are obtained from the rates (2.22) as

$$
\begin{aligned}
\dot{\omega}_{\mathrm{CH_4}} &= -\frac{W_{\mathrm{CH_4}}}{W_{\mathrm{O}}} \dot{\omega}_{\mathrm{I}}, \\
\dot{\omega}_{\mathrm{O_2}} &= -\frac{W_{\mathrm{O_2}}}{W_{\mathrm{O}}} \dot{\omega}_{\mathrm{IV}}, \\
\dot{\omega}_{\mathrm{H_2O}} &= \frac{W_{\mathrm{H_2O}}}{W_{\mathrm{O}}} (2\dot{\omega}_{\mathrm{IV}} - \dot{\omega}_{\mathrm{II}} - \dot{\omega}_{\mathrm{I}}), \\
\dot{\omega}_{\mathrm{CO_2}} &= \frac{W_{\mathrm{CO_2}}}{W_{\mathrm{O}}} \dot{\omega}_{\mathrm{II}}, \\
\dot{\omega}_{\mathrm{CO}} &= \frac{W_{\mathrm{CO}}}{W_{\mathrm{O}}} (\dot{\omega}_{\mathrm{I}} - \dot{\omega}_{\mathrm{II}}), \\
\dot{\omega}_{\mathrm{H_2}} &= \frac{W_{\mathrm{H_2}}}{W_{\mathrm{O}}} (4\dot{\omega}_{\mathrm{I}} + \dot{\omega}_{\mathrm{II}} + \dot{\omega}_{\mathrm{III}} - 3\dot{\omega}_{\mathrm{IV}}), \\
\dot{\omega}_{\mathrm{H}} &= 2\frac{W_{\mathrm{H}}}{W_{\mathrm{O}}} (\dot{\omega}_{\mathrm{IV}} - \dot{\omega}_{\mathrm{I}} - \dot{\omega}_{\mathrm{III}}).
\end{aligned}
\tag{2.23}
$$

We should mention that, although we have restricted our numerical computations to the case of reduced chemistry model, the techniques developed in this paper can be extended to general detailed chemical mechanisms without major conceptual modifications.

2.3. Moment M_1 model for radiative transfer

In many practical applications, solving the radiative transfer equation (2.6) is computationally very demanding and moment-based approximations are selected to speed up the computations. As an example of these approximations we consider the entropy M_1 model [1,14,2]. In order to formulate the M_1 model associated with the radiative transfer equation (2.6) we define the first three angular moments of the radiative intensity as

$$E = \frac{1}{c} \int_{\mathbb{S}^2} I \, \mathrm{d}\Omega, \quad \mathbf{F} = \frac{1}{c} \int_{\mathbb{S}^2} c\Omega I \, \mathrm{d}\Omega, \quad \mathbf{P} = \frac{1}{c} \int_{\mathbb{S}^2} \Omega \otimes \Omega I \, \mathrm{d}\Omega. \tag{2.24}$$

Here, $E(t, v, \mathbf{x})$ is the spectral radiative energy, $\mathbf{F}(t, v, \mathbf{x})$ the spectral radiative flux vector and $\mathbf{P}(t, v, \mathbf{x})$ the spectral radiative pressure tensor. Integrating (2.6) over all directions Ω, we obtain its zeroth-moment

$$\partial_t E + \tau \nabla \cdot \mathbf{F} = -c\sigma(E - 4\pi B(T, v)). \tag{2.25}$$

This equation is the spectral radiative energy balance equation. Next, multiplying (2.6) by Ω and integrating over all directions, we obtain its first-moment

$$\partial_t \mathbf{F} + \tau c^2 \nabla \cdot \mathbf{P} = -c\sigma \mathbf{F}. \tag{2.26}$$

This equation is the spectral radiative momentum balance equation.

Eqs. (2.25) and (2.26) are the basis of all angular moments models. However, the system they form is not closed (there are more unknowns than equations). To close it, we need an assumption on the radiative pressure so that we can write it as a function of the radiative energy and radiative flux. In the case of M_1 model [4,3], we use a maximum entropy principle. The radiative entropy is given by

$$\hbar(I) = \frac{2kv^2}{c^3}\left[(n_I+1)\ln(n_I+1) - n_I\ln(n_I)\right] \quad \text{with } n_I = \frac{c^2}{2hv^3}I.$$

With this definition, we can express the spectral M_1 closure function $\hat{I}$ as the maximum of the radiative entropy among the functions whose first two moments are E and $\mathbf{F}$,

$$H(\hat{I}) = \max_I\left\{H(I) = \frac{1}{c}\int_{\mathbb{S}^2}\hbar(I)\,\mathrm{d}\Omega\,\mathrm{d}v: \quad \frac{1}{c}\int_{\mathbb{S}^2}I\,\mathrm{d}\Omega = E \text{ and } \frac{1}{c}\int_{\mathbb{S}^2}c\Omega I\,\mathrm{d}\Omega = \mathbf{F}\right\}.$$

Solving this maximization problem, we get the form of the closure

$$\hat{I} = \frac{2hv^3}{c^2}\left(\mathrm{e}^{hv/k\Omega^T\cdot\mathbf{A}} - 1\right)^{-1},$$

where $\mathbf{A}$ is set so that the first two moments of the closure function are E and $\mathbf{F}$. It is now possible to close the system (2.25) and (2.26) expressing the radiative pressure as the second moment of our closure function. This leads to the Eddington form

$$\mathbf{P} = \mathbf{D}E, \tag{2.27}$$

where the Eddington tensor $\mathbf{D}$ is given by

$$\mathbf{D} = \frac{1-\chi(\mathbf{f})}{2}\mathbb{I} + \frac{3\chi(\mathbf{f})-1}{2}\frac{\mathbf{F}\otimes\mathbf{F}}{\|\mathbf{F}\|^2}, \quad \chi(\mathbf{f}) = \frac{3+4|\mathbf{f}|^2}{5+2\sqrt{4-3|\mathbf{f}|^2}}, \tag{2.28}$$

with $\mathbb{I}$ is the identity matrix, χ the Eddington factor and $\mathbf{f} = \frac{\mathbf{F}}{cE}$ the normalized flux. Hence, the equations to solve for the M_1 model are

$$\partial_t E + \tau\nabla\cdot\mathbf{F} = -c\sigma(E - 4\pi B(T,v)),$$
$$\partial_t\mathbf{F} + \tau c^2\nabla\cdot\mathbf{P} = -c\sigma\mathbf{F}, \tag{2.29}$$

where the radiative pressure $\mathbf{P}(E,\mathbf{F})$ is defined in (2.27). Note that the M_1 model (2.29) is hyperbolic, conserves the energy, locally decreases the total entropy, preserves the positivity of the radiative energy, satisfies the diffusion limit, and has a natural limitation of the flux i.e., $\|\mathbf{f}\| \leq 1$. The flux limited characteristic ensures that any radiative signal is propagated at a velocity below the speed of light. These properties are interesting and are required in many physical application in radiation hydrodynamics. We should mention that the well-known diffusion and P_N models do not satisfy these properties, compare [29] for numerical comparisons. For instance, in diffusion models, the signal is allowed to propagate at any arbitrarily high speed.

3. Solution procedure and numerical methods

Due to the absence of angular variable in radiation model, the structure of the partial differential equations in the combined low-Mach flows and M_1 model allow for consistent discretization tools to be used for both flow and radiation. Three stages namely, flow stage, combustion stage, and radiation stage are required for numerical solution of the coupled equations (2.16) and (2.29). In the current work, we use a modified projection method based on the MAC scheme which is similar to that used in [7,33] as an extension of the MAC scheme [38] for incompressible flows. The essential differences are in the use of extra source term and the inclusion of radiation and chemical effects. The M_1 equations (2.29) are solved using an HLL method in the same mesh structure as the one used in flow solution. In order to explain the steps required for a solution procedure, we divide the time interval into subintervals $[t_n, t_{n+1}]$ with $t_n = n\Delta t$ and we denote by Ψ^n the value of a generic function Ψ at time t_n. The procedure to advance the solution from the time t_n to the next time t_{n+1} can be carried out in the following steps:

Step 1. Radiation stage:
i. Solve for E^{n+1} and $\mathbf{F}^{n+1}$

$$\frac{E^{n+1} - E^n}{\Delta t} + \tau \nabla \cdot \mathbf{F}^n = -c\sigma(E^{n+1} - 4\pi B(T^n, v)),$$

$$\frac{\mathbf{F}^{n+1} - \mathbf{F}^n}{\Delta t} + \tau c^2 \nabla \cdot \mathbf{P}^n = -c\sigma \mathbf{F}^{n+1},$$

(3.1)

ii. Calculate the radiative heat term

$$q_{\mathrm{R}}^{n+1} = \tau c \int_0^\infty \sigma(4\pi B(T^n, v) - E^{n+1})\, \mathrm{d}v.$$

(3.2)

Step 2. Combustion stage:

i. For $i = 1, 2, \ldots N_{\mathrm{s}}$, update the mass fractions Y_i^{n+1}

$$\frac{Y_i^{n+1} - Y_i^n}{\Delta t} + \mathbf{u}^n \cdot \nabla Y_i^n + Y_i^n Q^n - \frac{1}{Re\,Sc}\nabla^2 Y_i^{n+1} - Da\dot{w}_i^n = 0.$$

(3.3)

ii. Update the reaction rates $\dot{\omega}_i^{n+1}$ according to (2.23) and calculate the chemical heat term

$$q_{\mathrm{C}}^{n+1} = \sum_{i=1}^{N_{\mathrm{s}}} \dot{\omega}_i^{n+1}.$$

(3.4)

Step 3. Flow stage:

i. Formulate the intermediate source term Q^*

$$Q^* = \frac{1}{p_0 Pr\,Re}\nabla^2 T^n - \frac{1}{\gamma p_0}q_{\mathrm{R}}^{n+1} + q_{\mathrm{C}}^{n+1}.$$

(3.5)

ii. Update the density ρ^{n+1}

$$\frac{\rho^{n+1} - \rho^n}{\Delta t} + \mathbf{u}^n \cdot \nabla \rho^n + \rho^n Q^* = 0.$$

(3.6)

iii. Update the temperature T^{n+1}

$$T^{n+1} = \frac{p_0}{\rho^{n+1}}.$$

(3.7)

iv. Formulate the source term Q^{n+1}

$$Q^{n+1} = \frac{1}{p_0 Pr\,Re}\nabla^2 T^{n+1} - \frac{1}{\gamma p_0}q_{\mathrm{R}}^{n+1} + q_{\mathrm{C}}^{n+1}.$$

(3.8)

v. Calculate the auxiliary velocity $\mathbf{u}^*$

$$\frac{\mathbf{u}^* - \mathbf{u}^n}{\Delta t} + \mathbf{u}^n \cdot \nabla \mathbf{u}^n - Q^{n+1}\mathbf{u}^n - \frac{1}{Re}\frac{1}{\rho^{n+1}}\left(\nabla^2 \mathbf{u}^n + \frac{1}{3}\nabla Q^{n+1}\right) = 0.$$

(3.9)

vi. Solve for the pressure p^{n+1}

$$-\nabla \cdot \left(\frac{\Delta t}{\rho^{n+1}}\nabla p^{n+1}\right) = Q^{n+1} - \nabla \cdot \mathbf{u}^*.$$

(3.10)

vii. Update the velocity $\mathbf{u}^{n+1}$

$$\mathbf{u}^{n+1} = \mathbf{u}^* - \frac{\Delta t}{\rho^{n+1}}\nabla p^{n+1}.$$

(3.11)

Notice that we have assumed no outer compression in the flow system such that the pressure appeared in (3.5), (3.7) and (3.8) is a constant i.e., $p_0 = p^{(0)}$. For closed systems, this pressure should be obtained by solving the ordinary differential equation (2.10). Note that the Poisson problem (3.10) is obtained by taking the divergence of (3.9) and using the fact that $\nabla \cdot \mathbf{u} = Q$. In the solution procedure, only one linear system has to be

solved at each time step to update the pressure p^{n+1} from (3.10). We should also point out that the reaction rates $\dot{\omega}_i^n$ and the source term Q^n in (3.3) contain the explicit temperature variable T^n. It is possible to treat these terms implicitly by solving first the flow stage followed by the combustion stage. In the considered test examples, both treatment produce the same results. Another way to solve the above equations is to involve all the stages implicitly in time. This procedure leads to a coupled nonlinear system to be solved at each time step. However, the numerical solution of such nonlinear system is computationally demanding and may limit the efficiency of the algorithm.

3.1. Space discretization

The space discretization of differential operators in the flow and combustion stages is performed using a staggered grid in which the different variables are located at different gridpoints as shown in Fig. 1 for a two-dimensional situation. This type of meshes, widely used in computational fluid dynamics, stabilizes the numerical method and guarantees that the computed flow solution is not perturbed by spurious pressure modes. All the second-order spatial derivatives are discretized using the central difference method whereas, upwind differencing is used for the first order spatial derivatives. Details on the implementation of these methods are given in [7,33] and will not be repeated here.

In this section, we focus our attention on the spatial discretization of the M_1 model. For two-dimensional problems, the M_1 model (2.29) becomes

$$
\begin{aligned}
&\frac{\partial E}{\partial t} + \tau \frac{\partial F^x}{\partial x} + \tau \frac{\partial F^y}{\partial y} = -c\sigma(E - 4\pi B(T, v)), \\
&\frac{\partial F^x}{\partial t} + \tau c^2 \frac{\partial P^{xx}}{\partial x} + \tau c^2 \frac{\partial P^{xy}}{\partial y} = -c\sigma F^x, \\
&\frac{\partial F^y}{\partial t} + \tau c^2 \frac{\partial P^{yx}}{\partial x} + \tau c^2 \frac{\partial P^{yy}}{\partial y} = -c\sigma F^y,
\end{aligned}
\tag{3.12}
$$

where radiative flux $\mathbf{F} = (F^x, F^y)^{\mathrm{T}}$, the Eddington factor $\mathbf{f} = (f^x, f^y)^{\mathrm{T}}$ and the radiative pressure

$$
\begin{aligned}
P^{xx} &= \left(\frac{1 - \chi(f^x, f^y)}{2} + \frac{3\chi(f^x, f^y) - 1}{2} \frac{F^x F^x}{(F^x)^2 + (F^y)^2} \right) E, \\
P^{xy} &= P^{yx} = \left(\frac{3\chi(f^x, f^y) - 1}{2} \frac{F^x F^y}{(F^x)^2 + (F^y)^2} \right) E, \\
P^{yy} &= \left(\frac{1 - \chi(f^x, f^y)}{2} + \frac{3\chi(f^x, f^y) - 1}{2} \frac{F^y F^y}{(F^x)^2 + (F^y)^2} \right) E,
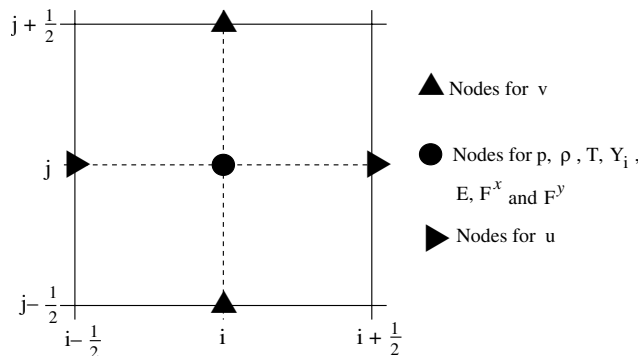\end{aligned}
\tag{3.13}
$$

with

Fig. 1. Staggered grid for two-dimensional space discretization.

$$f^x = \frac{F^x}{cE}, \quad f^y = \frac{F^y}{cE}, \quad \chi(f^x, f^y) = \frac{3 + 4((f^x)^2 + (f^y)^2)}{5 + 2\sqrt{4 - 3((f^x)^2 + (f^y)^2)}}.$$

Eqs. (3.12) can be rewritten as a system of conservation laws with source term

$$\frac{1}{\tau c} \frac{\partial \mathbf{U}}{\partial t} + \frac{\partial \mathbf{F}(\mathbf{U})}{\partial x} + \frac{\partial \mathbf{G}(\mathbf{U})}{\partial y} = -\frac{1}{\tau} \mathbf{R}(\mathbf{U}), \tag{3.14}$$

where

$$\mathbf{U} = \begin{pmatrix} E \\ F^x \\ F^y \end{pmatrix}, \quad \mathbf{F}(\mathbf{U}) = \begin{pmatrix} \frac{F^x}{c} \\ cP^{xx} \\ cP^{yx} \end{pmatrix}, \quad \mathbf{G}(\mathbf{U}) = \begin{pmatrix} \frac{F^y}{c} \\ cP^{xy} \\ cP^{yy} \end{pmatrix}, \quad \mathbf{R}(\mathbf{U}) = \begin{pmatrix} \sigma(E - 4\pi B(T)) \\ \sigma F^x \\ \sigma F^y \end{pmatrix}.$$

It is easy to verify that the Jacobian matrices associated with flux functions $\mathbf{F}(\mathbf{U})$ and $\mathbf{G}(\mathbf{U})$ are given by

$$\begin{pmatrix} 0 & 1 & 0 \\ \frac{(2f^2 - 3(f^y)^2)(\chi - f\chi') + (f^y)^2}{f^2} & \frac{f^x(f^y)^2(6\chi - 3f\chi' - 2)}{2f^4} + \frac{f^y}{f} & \frac{f^y(f^x)^2(1 - 3\chi + f\chi')}{f^4} - \frac{(f^y)^3\chi'}{2f^3} \\ \frac{3f^xf^y(\chi - f\chi') - 1}{2f^2} & \frac{f^y(f^x)^2(3f\chi' - 3\chi - 1) - 3(f^y)^3(1 + \chi)}{2f^4} & \frac{3f^x(f^y)^2(f\chi' + \chi - 1) + (f^x)^3(3\chi - 1)}{2f^4} \end{pmatrix},$$

and

$$\begin{pmatrix} 0 & 1 & 0 \\ \frac{(2f^2 - 3(f^x)^2)(\chi - f\chi') + (f^x)^2}{f^2} & \frac{f^y(f^x)^2(6\chi - 3f\chi' - 2)}{2f^4} + \frac{f^x}{f} & \frac{f^x(f^y)^2(1 - 3\chi + f\chi')}{f^4} - \frac{(f^x)^3\chi'}{2f^3} \\ \frac{3f^xf^y(\chi - f\chi') - 1}{2f^2} & \frac{f^x(f^y)^2(3f\chi' - 3\chi - 1) - 3(f^x)^3(1 + \chi)}{2f^4} & \frac{3f^y(f^x)^2(f\chi' + \chi - 1) + (f^y)^3(3\chi - 1)}{2f^4} \end{pmatrix},$$

respectively. The eigenvalues of the matrix $\frac{\partial \mathbf{F}(\mathbf{U})}{\partial \mathbf{U}}$ are given by

$$\lambda^{\pm} = c\left(\frac{f^x}{\xi} \pm \frac{\sqrt{2}\sqrt{(\xi - 1)(\xi + 2)(2(\xi - 1)(\xi + 2) + 3(f^y)^2)}}{\sqrt{3}\xi(\xi + 2)}\right), \quad \lambda^0 = c\frac{(2 - \xi)f^x}{f^2},$$

with $\xi = \sqrt{4 - 3f^2}$ and $f^2 = (f^x)^2 + (f^y)^2$. Analogously, the eigenvalues of the matrix $\frac{\partial \mathbf{G}(\mathbf{U})}{\partial \mathbf{U}}$ are

$$\beta^{\pm} = c\left(\frac{f^y}{\xi} \pm \frac{\sqrt{2}\sqrt{(\xi - 1)(\xi + 2)\left(2(\xi - 1)(\xi + 2) + 3(f^x)^2\right)}}{\sqrt{3}\xi(\xi + 2)}\right), \quad \beta^0 = c\frac{(2 - \xi)f^y}{f^2}.$$

Using the same mesh structure as the one used in hydrodynamics shown in Fig. 1, a semi-discrete M_1 model reads

$$\frac{1}{\tau c} \frac{d\mathbf{U}_{i,j}}{dt} + \frac{\mathscr{F}_{i+\frac{1}{2},j} - \mathscr{F}_{i-\frac{1}{2},j}}{\Delta x} + \frac{\mathscr{G}_{i,j+\frac{1}{2}} - \mathscr{G}_{i,j-\frac{1}{2}}}{\Delta y} = -\frac{1}{\tau} \mathbf{R}(\mathbf{U}_{i,j}), \tag{3.15}$$

where the numerical fluxes $\mathscr{F}_{i+\frac{1}{2},j}$ and $\mathscr{G}_{i,j+\frac{1}{2}}$ have to be reconstructed such that the discretization (3.15) is consistent to the one used to discretize the low-Mach equations in (2.16). Furthermore, it is required that discretization method should be monotone and preserve positivity and flux limitation properties. The exact Riemann solver for M_1 equations is generally considered too expensive for most Godunov type methods. As a result, several approximate Riemann solvers have been developed. One of the most widely used solvers is the Roe approximate Riemann solver [25]. The Roe's solver requires eigen-decomposition, which becomes more complicated and time consuming in radiation transport. Furthermore, the Roe's approximate Riemann solver does not preserve the positivity.

The HLL approximate Riemann solver proposed in [9] provides a positive scheme if used with an appropriate choice of wavespeed bounds for any hyperbolic system. Moreover, the HLL Riemann solver does not require field-decomposition. Applied to the semi-discrete problem (3.15), the HLL reconstruction gives

$$\mathscr{F}_{i+\frac{1}{2},j} = \frac{a^+_{i+\frac{1}{2},j}\mathbf{F}_{i,j} - a^-_{i-\frac{1}{2},j}\mathbf{F}_{i+1,j}}{a^+_{i+\frac{1}{2},j} - a^-_{i-\frac{1}{2},j}} + \frac{a^+_{i+\frac{1}{2},j}a^-_{i-\frac{1}{2},j}}{a^+_{i+\frac{1}{2},j} - a^-_{i-\frac{1}{2},j}}(\mathbf{U}_{i,j} - \mathbf{U}_{i+1,j}),$$

$$\mathscr{G}_{i,j+\frac{1}{2}} = \frac{b^+_{i,j+\frac{1}{2}}\mathbf{G}_{i,j} - b^-_{i,j-\frac{1}{2}}\mathbf{G}_{i,j+1}}{b^+_{i,j+\frac{1}{2}} - b^-_{i,j-\frac{1}{2}}} + \frac{b^+_{i,j+\frac{1}{2}}b^-_{i,j-\frac{1}{2}}}{b^+_{i,j+\frac{1}{2}} - b^-_{i,j-\frac{1}{2}}}(\mathbf{U}_{i,j} - \mathbf{U}_{i,j+1}),$$

$$(3.16)$$

where the characteristic speeds $a^\pm_{i+\frac{1}{2},j}$ and $b^\pm_{i,j+\frac{1}{2}}$ are defined as

$$a^+_{i+\frac{1}{2},j} = \max\left(0, \lambda^+_{i,j}, \lambda^+_{i+1,j}\right), \quad a^-_{i+\frac{1}{2},j} = \min\left(0, \lambda^-_{i,j}, \lambda^-_{i+1,j}\right),$$

$$b^+_{i,j+\frac{1}{2}} = \max\left(0, \beta^+_{i,j}, \beta^+_{i,j+1}\right), \quad b^-_{i,j+\frac{1}{2}} = \min\left(0, \beta^-_{i,j}, \beta^-_{i,j+1}\right).$$

$$(3.17)$$

Once the numerical fluxes in (3.16) are reconstructed, the time integration of the semi-discrete equations (3.15) is performed using the semi-implicit scheme (3.1).

4. Results and numerical examples

The presented low-Mach asymptotic for fluid dynamics was verified in Ref. [33] using the same discretization methods as those presented in the current work. In [33] the well-known procedure of manufacturing solutions has been considered. The numerical results obtained with low-Mach model and the exact manufactured solution were in perfect agreement. Therefore, we will not present these results here. In this section, three test examples with different range of difficulties have been selected to check the performance of the proposed coupled radiation hydrodynamics. We first consider a static purely radiative transfer, next we solve the natural convection with large temperature difference in non-reacting gray medium. In the last example, we test our methods for a diffusion methane/air flame with non-gray chemical species.

4.1. Static purely radiative problem

As a first test example we consider radiative transfer in a static gray fluid contained in the unit square $\mathscr{D} = [0,1] \times [0,1]$. This corresponds on solving Eqs. (2.29) with gray Plank function

$$B(T) = \sigma_R T^4, \tag{4.1}$$

where $\sigma_R = 5.67 \times 10^{-8}$ is the Boltzmann constant. Non-dimensional quantities are used such that the radiative speed $c = 1$. We also assume that a thermodynamic equilibrium holds such that the fluid temperature and the radiation temperature are equal i.e., $E = 4\pi B(T)$. Thus, the term in the right hand side of the first equation in (2.29) vanishes and the optical thickness τ is the only free parameter in the problem considered. Notice that the absorption coefficient is related to τ by the definition (2.3) with $x_{ref} = 1$. On the boundary $\partial\mathscr{D}$ we use

$$E = 4\pi B(T_w), \quad F^x = F^y = 0,$$

where T_w is the wall temperature. Here, only the bottom wall is heated at $T = 1000$ and the other remaining walls are fixed at $T = 300$. Initially, $E = 4\pi B(300)$, $F^x = F^y = 0$ and steady-state results are presented. The time stepping is stopped when the relative L^∞−error in the radiative energy is less than 10^{-7}. Two cases are studied in terms of the optical thickness, namely $\tau = 1$ and $\tau = 0.1$. Our objective from this example is to verify the performance of the M_1 model compared to a direct solver for the radiative transfer equation (2.6). To this end we solve the radiative transfer equation (2.6) using the well-established diffusion synthetic acceleration (DSA) method. The DSA method uses the diffusion approach to accelerate the source iteration which has been widely used in computational radiative transfer, we refer to [30,28] for the implementation of the method and further discussions on other direct methods can found therein. The S_8 discrete-ordinate algorithm is selected for the discretization of angle variable and a mesh of 100×100 is used in our computations.

Fig. 2 contains level curves for the normalized radiative energy, $\mathbb{E} = E/B(1000)$, for $\tau = 1$ and $\tau = 0.1$. In this figure we show contours with 10 equally spaced contour lines from $\mathbb{E} = 0.045$ to $\mathbb{E} = 0.50$. An analysis of plots shows that the HLL scheme used to solve the M_1 model produces accurate solutions which are very close
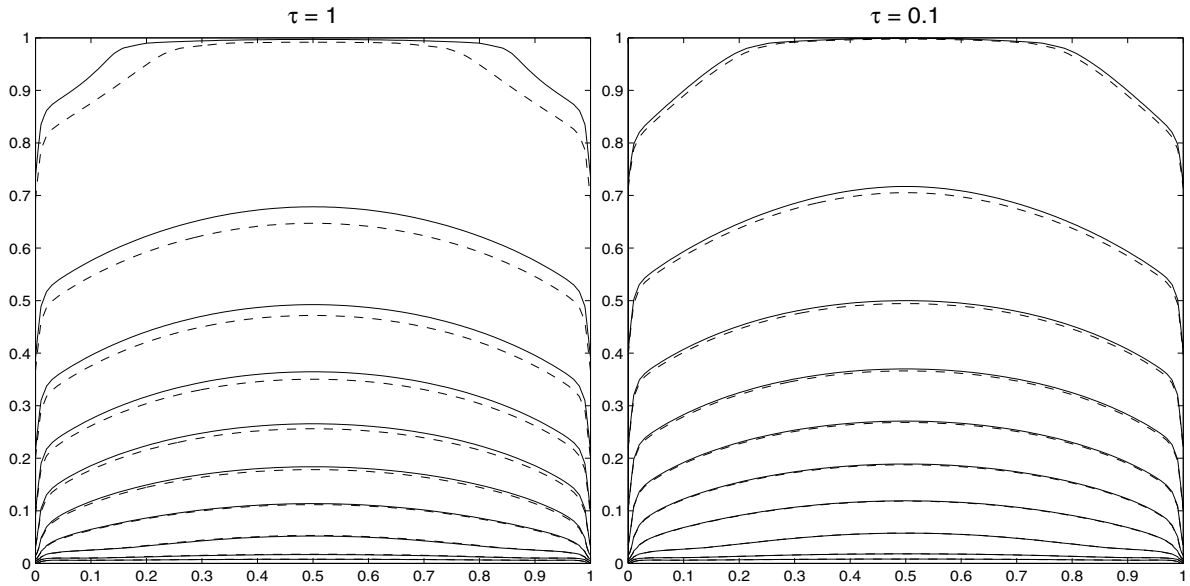
$\tau = 1$ $\tau = 0.1$

Fig. 2. Contours of the normalized radiative energy for $\tau = 1$ (left) and $\tau = 0.1$ (right). The solid and dashed lines present the results obtained using the radiative transfer and the M_1 model, respectively.

to the direct solution of radiative transfer equations. For $\tau = 1$ there is a reasonable agreement with the results obtained using the M_1 model and those obtained using the direct solver. At low optical thickness the discrepancies between the direct solver and the M_1 model are very small since the radiative regime is diffusive and the M_1 model can be a good candidate for such situations. It should be noted that approximately 2422 and 18,003 steps are needed to reach a steady-state solution for $\tau = 1$ and $\tau = 0.1$, respectively.

To give an idea about the CPU times, Table 2 summarizes some of them for $\tau = 1$ and $\tau = 0.1$, where the computations were made in a Pentium IV 2.66 GHz having 1Gb of RAM. The codes only take the default optimization of the machine, i.e. they are not parallel codes. We have listed computational timings for the DSA algorithm using the S_4 discrete-ordinate set (containing 24 directions in the unit sphere) and the S_8 (with 80 ordinates). It is obvious that increasing the number of directions in S_n discrete-ordinate sets results in an increase of the computational cost for the DSA algorithm. As expected, in all presented simulations the M_1 model is faster than the DSA method for both values of τ. A balance between the accuracy reported in Fig. 2 and the computational work listed in Table 2 benefits the M_1 model. As efficiency is particularly important in the development of radiative simulation codes, the M_1-radiation model used is not only realistic enough to yield meaningful calculations, but also simple and fast enough to avoid overcharging the computational cost.

4.2. Natural convection with large temperature difference

The natural convection in a squared cavity with large temperature difference has been chosen to verify the performance of the M_1 model for low-Mach number flow in non-reacting gray medium. This test example has been used in several numerical studies in CFD, see [15,24] among others. The purpose of the present example is to study the radiation–convection interaction in natural convection by using the M_1 model. Here, the flow domain is a squared cavity with dimension L while the left and right vertical walls are maintained at hot tem-

Table 2
CPU times (in seconds) for the static purely radiative problem

	DSA using S_4-set	DSA using S_8-set	M_1 model
$\tau = 1$	49.3	174.1	36.7
$\tau = 0.1$	581.6	2440.8	298.0

perature T_H and cold temperature T_C, respectively. The bottom and top horizontal walls are insulated. Using the notation shown in Fig. 3, the boundary conditions are

$$
\begin{aligned}
&T(t,\hat{\mathbf{x}}) = T_\mathrm{H}, \quad E(t,\hat{\mathbf{x}}) = 4\pi B(T_\mathrm{H}), \quad \forall \hat{\mathbf{x}} \in \Gamma_\mathrm{H}, \\
&T(t,\hat{\mathbf{x}}) = T_\mathrm{C}, \quad E(t,\hat{\mathbf{x}}) = 4\pi B(T_\mathrm{C}), \quad \forall \hat{\mathbf{x}} \in \Gamma_\mathrm{C}, \\
&\mathbf{n}(\hat{\mathbf{x}}) \cdot \nabla T(t,\hat{\mathbf{x}}) = 0, \quad \mathbf{n}(\hat{\mathbf{x}}) \cdot \nabla E(t,\hat{\mathbf{x}}) = 0, \quad \forall \hat{\mathbf{x}} \in \Gamma, \\
&\mathbf{u}(t,\hat{\mathbf{x}}) = \mathbf{0}, \quad \mathbf{F}(t,\hat{\mathbf{x}}) = \mathbf{0}, \quad \forall \hat{\mathbf{x}} \in \Gamma_\mathrm{H} \cup \Gamma \cup \Gamma_\mathrm{C},
\end{aligned}
\tag{4.2}
$$

where $B(T)$ is the gray Planck function (4.1) and $\mathbf{n}(\hat{\mathbf{x}})$ denotes the outward unit normal in $\hat{\mathbf{x}}$ with respect to the boundary wall. The Rayleigh number, which is the parameter of interest in natural convection, is related to the Reynolds number by $Ra = Pr\,Re^2$. The local Nusselt number at the hot wall, Nu, and its averaged value, $\overline{Nu}$, are defined as

$$
Nu(y) = \frac{L}{T_\mathrm{H} - T_\mathrm{C}} \left.\frac{\partial T}{\partial x}\right|_{\Gamma_\mathrm{H}}, \quad \overline{Nu} = \frac{1}{L} \int_0^L Nu(y)\, \mathrm{d}y.
$$

In our computations, $L = 1$ m, $T_\mathrm{H} = 1000$ K, $T_\mathrm{C} = 300$ K, $Pr = 0.71$ and $Ra = 10^4$. The absorption coefficient σ and the optical thickness τ are both set to unity. We use a mesh with 100×100 gridpoints and steady-state results are presented. In Fig. 4, we display the isotherms for computations without radiation and with the M_1 model. As expected, due to buoyancy forces, the fluid rises from the hot wall and propagates towards the cold wall. The velocity vectors are presented in Fig. 5. The effects of radiation on both temperature distribution and flow field can clearly be seen from these figures. It is also noticeable that the thermal radiation alters the fluid motion inside the enclosure, compare the recirculation region and its location in Fig. 5. The low Mach asymptotic and the M_1 model accurately resolve this test problem.

For comparison reasons, we plot in Fig. 6 cross-sections of the u-velocity at mid-width cavity of $x = L/2$ and the v-velocity at mid-height cavity of $y = L/2$. Fig. 7 shows the cross-section of the temperature at mid-height cavity and the local Nusselt number at the hot wall. The local Nusselt number at the cold wall shows similar features and is not presented here. Along with the plots shown in Figs. 6 and 7, we have included the results obtained using the diffusion model. This model can be recovered from Eqs. (2.29) by setting the Eddington tensor $\mathbf{D} = \frac{1}{3}\mathbb{I}$ in (2.28). For steady-state computations this reduces to the diffusion equation

$$
-\tau^2 \nabla \cdot \left(\frac{1}{3\sigma} \nabla E \right) + \sigma E = 4\pi\sigma B(T),
\tag{4.3}
$$

to be solved for the radiative energy E only.

From a simple examination of Fig. 6 one observes that the effects of radiation on the velocity field are more pronounced near the hot wall becoming smaller close to the cold wall. The v-velocity component also shows
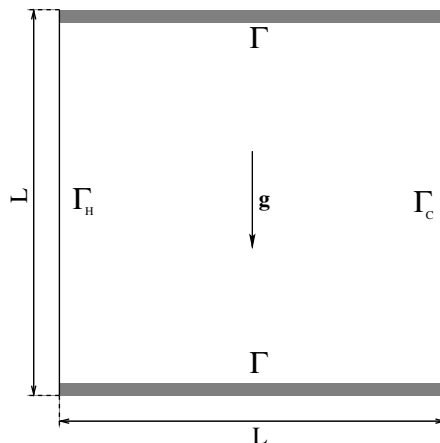

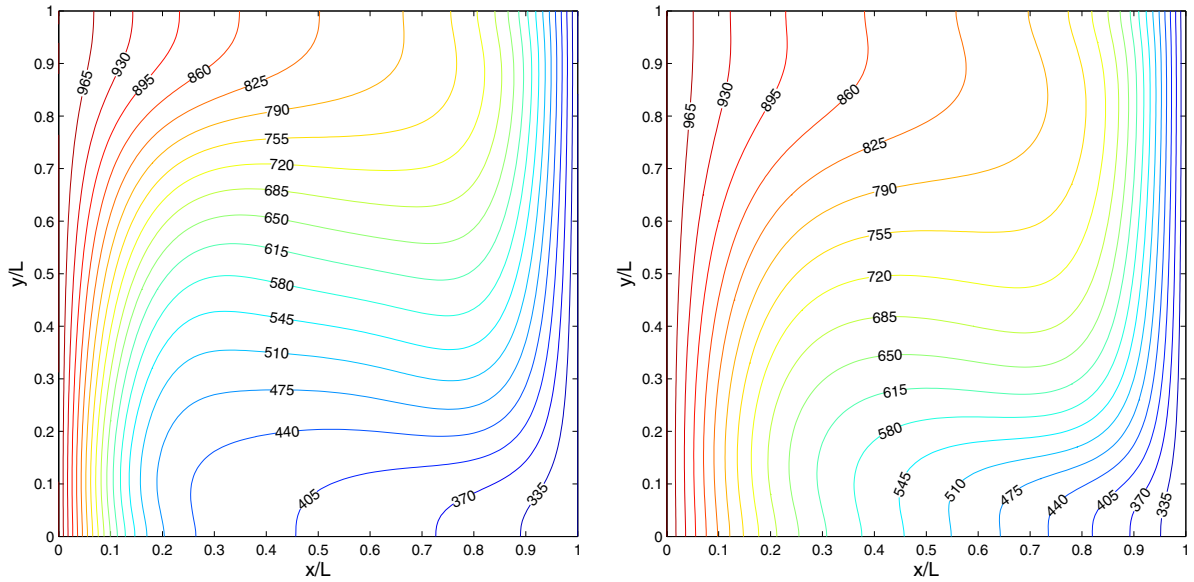Fig. 3. Schematic representation of natural convection in a squared cavity.

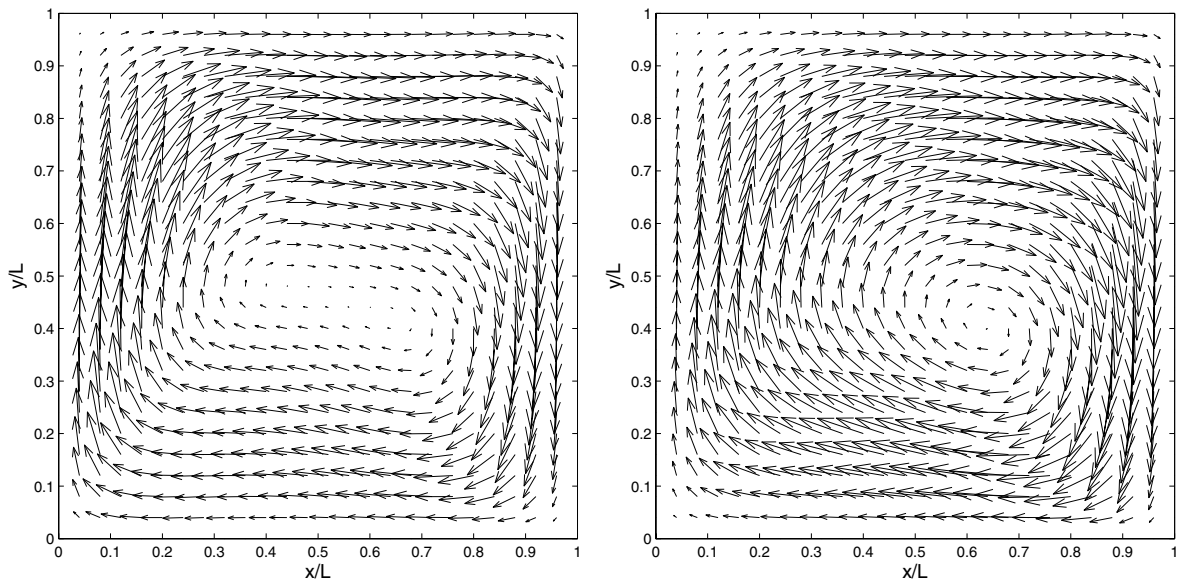Fig. 4. Isotherms for natural convection without radiation (left) and with M_1 model (right).

Fig. 5. Velocity field for natural convection without radiation (left) and with M_1 model (right).

large difference in the mid-plane of the cavity. Furthermore, when radiation is included the temperature increases in the center of the cavity, see Fig. 7. This can be explained by the fact that the radiative energy is proportional to the fourth power of absolute temperature, with the increase of temperature difference the radiative heat transfer between the hot wall and the closer regions becomes smaller than that between the other cold regions in the cavity.

The computed local Nusselt number in Fig. 6 confirms that about 13% of the heat released is radiated a way from the enclosure when radiation is accounted for by the M_1 model. It was concluded that, for the considered *Ra* number, the averaged Nusselt number $\overline{Nu} = 3.3833$ for the simulation without radiation and $\overline{Nu} = 2.0741$ for the M_1 model. It turns out that the averaged Nusselt number for the M_1 simulation is less that 38.69%
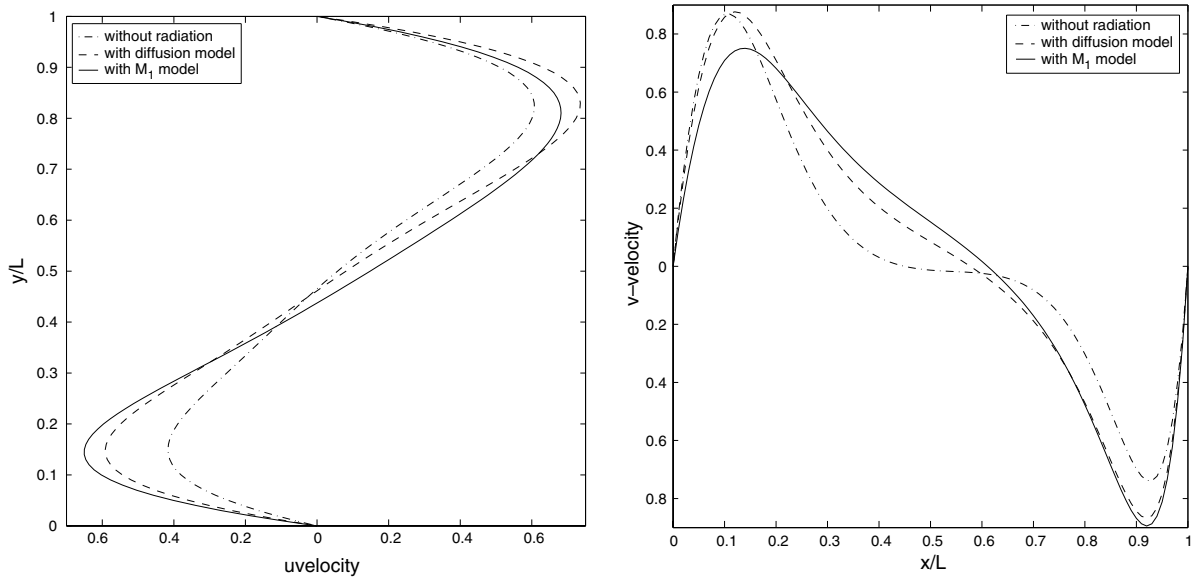
Fig. 6. Cross-section of the *u*-velocity at mid-width cavity (left) and the *v*-velocity at mid-height cavity (right).
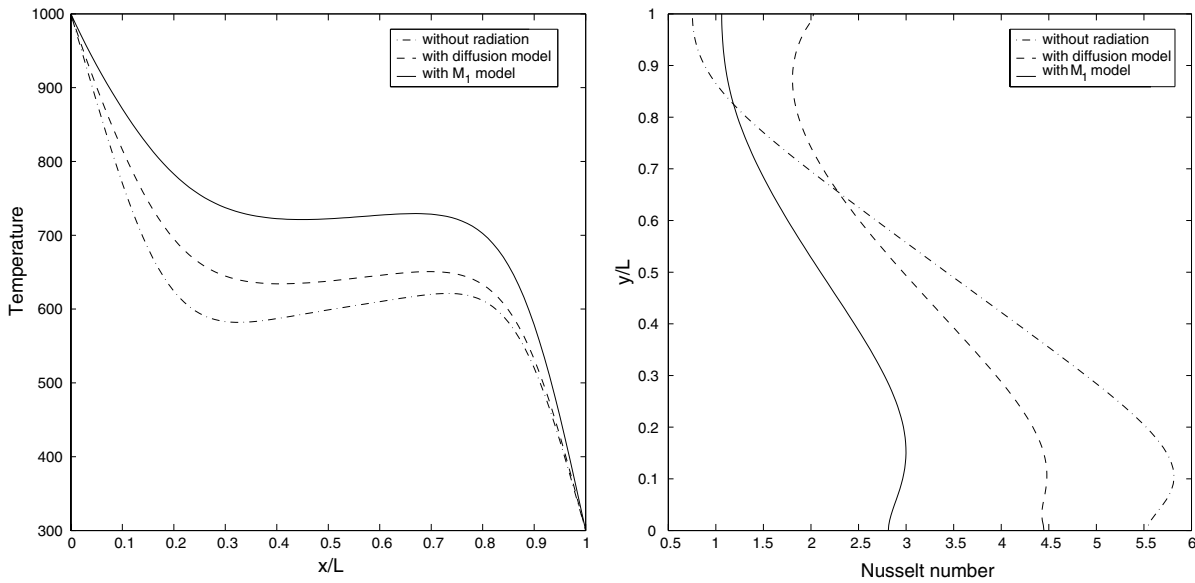

Fig. 7. Cross-section of the temperature at mid-height cavity (left) and local Nusselt number at the hot wall (right).

smaller than the averaged Nusselt number obtained by neglecting the interaction between convection and radiation. A CPU time would take around 63 min for no-radiation case and 74 min for the M_1 computations. From a computational stand point and regarding to the obtained results, the M_1 model can be considered as an efficient method for incorporating radiative effects in natural convection simulations.

4.3. Diffusion methane/air flame

The present example attempts to numerically examine a diffusion methane/air flame with and without consideration of the radiation effects. The M_1 model has been used for this purpose. Here, the proposed physical model consists of a two-dimensional enclosure containing a diffusion flame with the fuel injection diameter *D*

is taken as reference length, as sketched in Fig. 8. The width of the inner fuel region and outer air region are respectively, D and $2D$ while length and height of the computational domain are taken as $20D$ and $40D$, respectively. The burner is initially filled with air at room temperature and the flow is at rest. Fuel and air are both at room temperature are allowed to enter the system giving rise to combustion and the flame propagates to the burner exit. The velocities of the central fuel and the annular air jets are taken to be 10 and 5 m/s, respectively. The mass fraction of the species at the inlet is distributed according to the local equivalence ratio as shown in Table 3. Thermodynamic properties of chemical species, namely, molar concentration of species are taken from the database CHEMKIN-III [10]. The selected flame conditions and reference values for the evaluation of the present problem are summarized in Table 4. For this flame conditions, the Reynolds number $Re = 4000$, the Schmidt number $Sc = 0.93$, and the optical thickness $\tau = 0.5$.

In terms of radiative heat transfer, the species CO, CO_2 and H_2O are the most radiating species in methane/air diffusion flames. This due to their absorbing and emitting nature in participating media. In all the results presented here, the M_1 model with 15 groups is solved, see [35] for details on the 15 groups and their opacities.
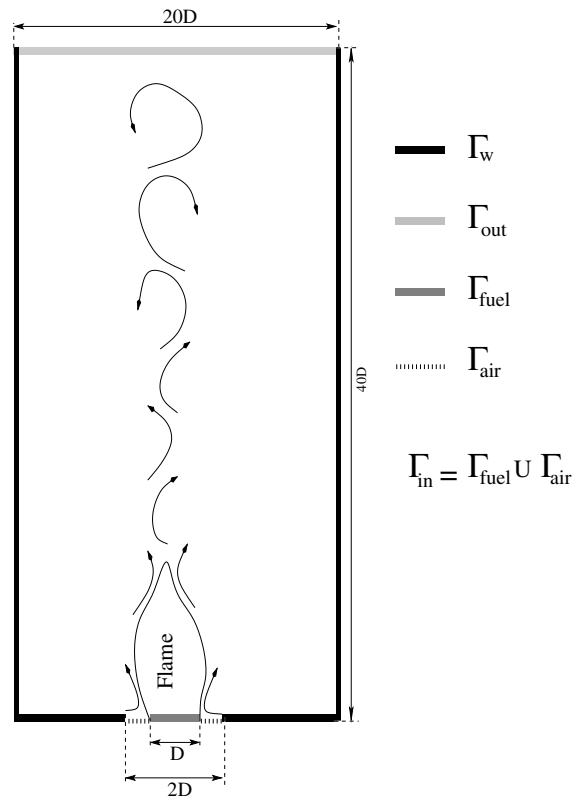

Fig. 8. Configuration for the two-dimensional diffusion flame.

Table 3
Composition of the gas used in methane/air flame

Species	Mass fraction (%)
N_2	69.239
O_2	0.0
C_4	1.776
CO	0.1
CO_2	18.899
H_2O	9.986

Table 4
Property parameters and reference quantities considered in the present study

Quantity	Unit	Symbol	Typical reference value
x, y	m	$x_{ref} = D$	1 m
u	m/s	u_{ref}	1 m/s
ρ	kg/m^3	ρ_{ref}	1.2 kg/m^3
g	m/s^2	g_{ref}	10 m/s^2
p	kg/ms^2	p_{ref}	10^5 Pa $= 10^5$ kg/ms^2
T	K	T_{ref}	300 K
σ	1/m	σ_{ref}	100/m
i	kg/s^3 sr	I_{ref}	258,480 kg/s^3 sr
R	m^2/K s^2		287 m^2/K s^2
c_p	m^2/K s^2		1005 m^2/K s^2
K	kg m/K s^2		25×10^{-3} kg m/K s^2
μ	kg/ms		18×10^{-6} kg/ms

The mean absorption coefficients are evaluated using the techniques described in [23]. Based on the notation depicted in Fig. 8, the boundary conditions for the flow variables are

$$
\begin{aligned}
&u(t, \hat{\mathbf{x}}) = u_{in}, \quad v(t, \hat{\mathbf{x}}) = 0 \quad \forall \hat{\mathbf{x}} \in \Gamma_{in}, \\
&u(t, \hat{\mathbf{x}}) = v(t, \hat{\mathbf{x}}) = 0 \quad \forall \hat{\mathbf{x}} \in \Gamma_w, \\
&\mathbf{n}(\hat{\mathbf{x}}) \cdot \nabla u(t, \hat{\mathbf{x}}) = \mathbf{n}(\hat{\mathbf{x}}) \cdot \nabla v(t, \hat{\mathbf{x}}) = 0 \quad \forall \hat{\mathbf{x}} \in \Gamma_{out}, \\
&T(t, \hat{\mathbf{x}}) = T_{in} \quad \forall \hat{\mathbf{x}} \in \Gamma_{in}, \\
&T(t, \hat{\mathbf{x}}) = T_w \quad \forall \hat{\mathbf{x}} \in \Gamma_w, \\
&\mathbf{n}(\hat{\mathbf{x}}) \cdot \nabla T(t, \hat{\mathbf{x}}) = 0 \quad \forall \hat{\mathbf{x}} \in \Gamma_{out}.
\end{aligned}
\tag{4.4}
$$

The inlet flow and temperature are defined such that $u_{in} = u_{fuel}$, $T_{in} = T_{fuel}$ on Γ_{fuel}, and $u_{in} = u_{air}$, $T_{in} = T_{air}$ on Γ_{air}. For the chemical species, we imposed the following boundary conditions

$$
\begin{aligned}
&Y_i(t, \hat{\mathbf{x}}) = Y_{i,in} \quad \forall \hat{\mathbf{x}} \in \Gamma_{in}, \\
&\mathbf{n}(\hat{\mathbf{x}}) \cdot \nabla Y_i(t, \hat{\mathbf{x}}) = 0 \quad \forall \hat{\mathbf{x}} \in \Gamma_w \cup \Gamma_{out},
\end{aligned}
\tag{4.5}
$$

with $Y_{i,in} = Y_{fuel}$ on Γ_{fuel} and $Y_{i,in} = Y_{air}$ on Γ_{air}. Finally, the boundary condition for radiative energy and flux are given as

$$
\begin{aligned}
&\mathbf{F}(t, \hat{\mathbf{x}}) = \mathbf{0} \quad \forall \hat{\mathbf{x}} \in \Gamma_{in} \cup \Gamma_w \cup \Gamma_{out}, \\
&E(t, \hat{\mathbf{x}}) = B(T_{in}, v) \quad \forall \hat{\mathbf{x}} \in \Gamma_{in}, \\
&E(t, \hat{\mathbf{x}}) = B(T_w, v) \quad \forall \hat{\mathbf{x}} \in \Gamma_w, \\
&\mathbf{n}(\hat{\mathbf{x}}) \cdot \nabla E(t, \hat{\mathbf{x}}) = 0 \quad \forall \hat{\mathbf{x}} \in \Gamma_{out}.
\end{aligned}
\tag{4.6}
$$

First we check the grid dependence of the computed solutions for this test problem. To this end we consider four uniform meshes with 50×100, 100×200, 200×400 and 400×800 gridpoints. On each mesh, we compute the mean temperature variation (MTV) defined as

$$
\mathrm{MTV} = \frac{1}{\bar{T}} \left(\sum_{i,j} \left(T_{ij} - \bar{T} \right)^2 \Delta x \Delta y \right)^{\frac{1}{2}} \quad \text{with } \bar{T} = \sum_{i,j} T_{ij} \Delta x \Delta y.
$$

The obtained MTV results are listed In Table 5 for simulations without radiation and with M_1 model at time $t = 0.004$ s and $t = 0.009$ s. It is easy to verify that for the last two meshes the differences in the MTV values reported in Table 5 are very small. For instance, the discrepancies in the maximum and minimum values of temperature on the mesh with 200×400 gridpoints and the mesh with 400×800 gridpoints are less than 0.3% at time $t = 0.004$ s. These differences become less than 0.8% at time $t = 0.009$ s. Similar behaviors have been observed for the other simulation times. Therefore, bearing in mind the slight change in the results from mesh with 200×400 gridpoints and mesh with 400×800 gridpoints at the expanse of rather significant in-

Table 5
The mean temperature variation for simulations without radiation and with M$_1$ model

Gridpoints	Without radiation		With M$_1$ model	
	$t = 0.004$ s	$t = 0.009$ s	$t = 0.004$ s	$t = 0.009$ s
50×100	0.4237	0.4512	0.4527	0.5013
100×200	0.3121	0.4116	0.3758	0.4534
200×400	0.3428	0.3993	0.3546	0.4078
400×800	0.3511	0.4002	0.3605	0.4101

crease in CPU times, the mesh with 200×400 gridpoints is believed to be appropriate to obtain the results free of grid effects. Hence, the results presented herein are based on the mesh with 200×400 gridpoints.

Fig. 9 illustrates the temperature distributions at times $t = 0.002, 0.004, 0.006, 0.009$ and 0.013 s. We present results for low-Mach simulations without radiation and for simultaneously occurring flow, combustion,
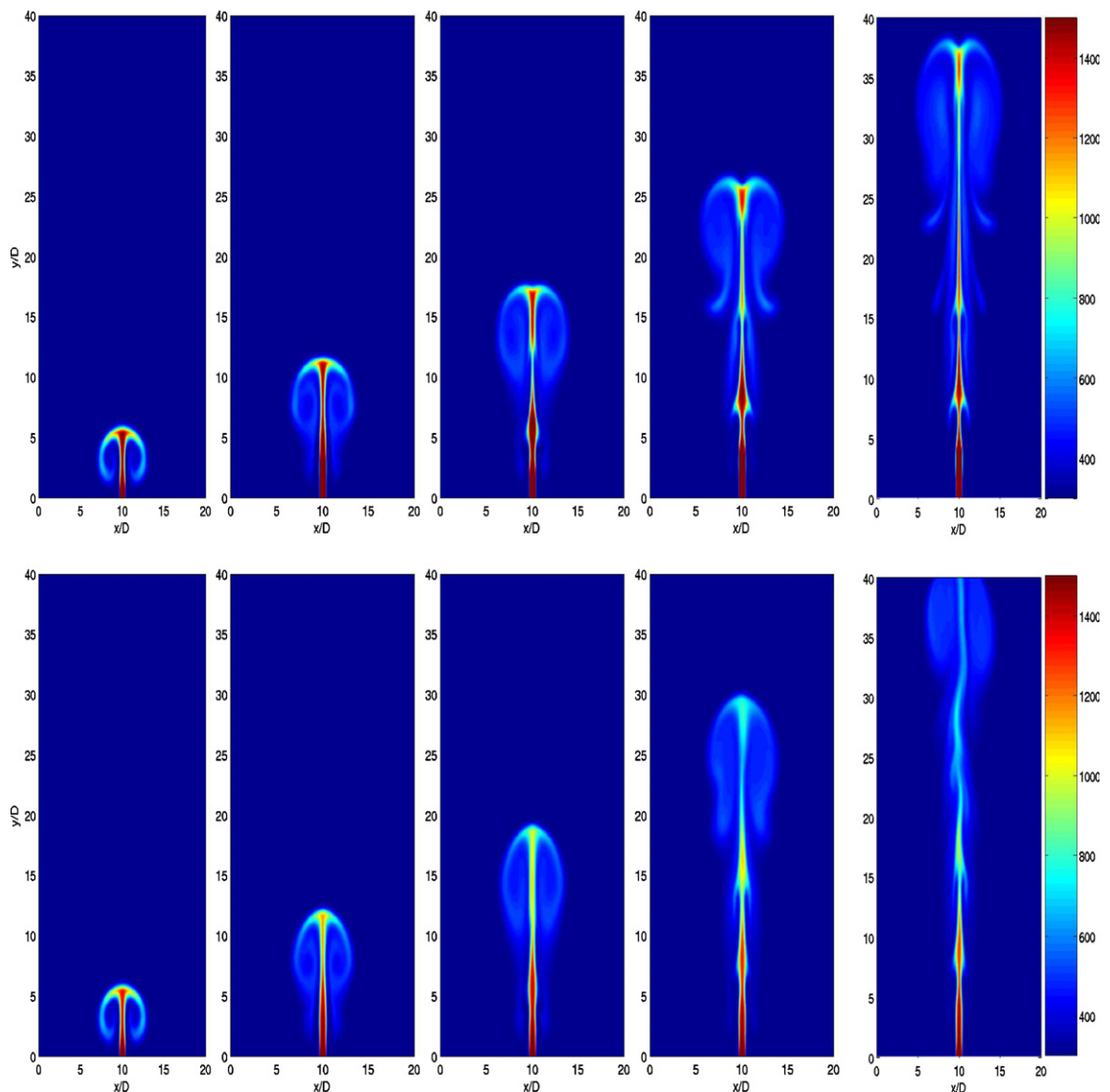

Fig. 9. Evolution of temperature distribution without radiation (upper row) and with M$_1$ model (lower row) at times (from left to right) $t = 0.002$, $t = 0.004$, $t = 0.006$, $t = 0.009$ and $t = 0.013$ s.

convection and M_1-radiation phenomena. It is clear that the inclusion of thermal radiation in the problem, by means of the M_1 model, has reduced the size of the flame region where maximum temperatures are located. Radiative heat transfer is also responsible for reducing the size of high temperature regions of the flame and for shifting them towards the furnace inlet. Moreover, the M_1 model simulates faster heat release, leading to a shorter flame. This model has increased the percentage of heat leaving through axial location of the flame, emphasizing the significance of the particular sink term, $\nabla \cdot q_R$, in the total energy balance. For the considered flame, ignoring the effects of thermal radiation causes cooler flame temperatures with a maximum error of about 350 K in the centerline region above the visible flame tip. It is also clear that the radiative heat flux is zero at the inlet of the burner because there is very little radiation since the temperature at the inlet is approximately that of the surroundings (300 K). Near the exit, the radiation out of the solid wall increases again for the reference case because this region is localized near the blackbody surroundings at 300 K.

In Fig. 10 we present the time evolution of velocity vectors for the no-radiation and the M_1-radiation simulations. At short time calculations, very little energy is needed to drive the flow compared with the experiment
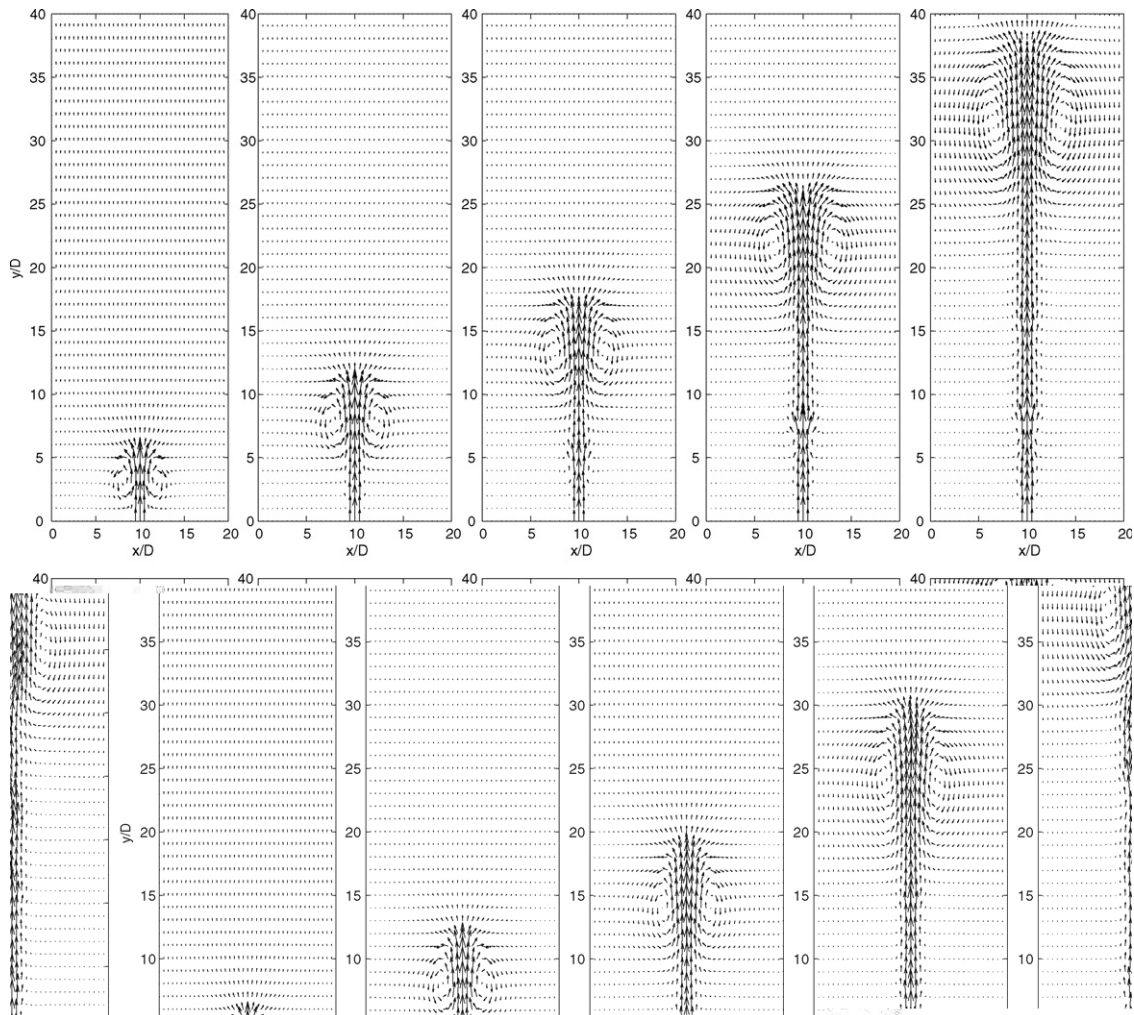

Fig. 10. Evolution of velocity field without radiation (upper row) and with M_1 model (lower row) at times (from left to right) $t = 0.002$, $t = 0.004$, $t = 0.006$, $t = 0.009$ and $t = 0.013$ s.

on the flow at large time simulations. We can observe that the velocity increases in the inlet region along the centerline due to the increase in temperature. The increased radial velocity provided an additional mechanism for mixing, so that the reaction zone become wider and the flame is shorter than that calculated without radiation. It can also be seen that two vortices are formed and have been advected within the flame front during the simulation process. The location of these weak recirculation zones within the flame domain indicates clearly that thermal radiation alters the gas flow in the enclosure. It is worth noting that when radiation is included in the enclosure, an asymmetric behavior is detected in the flame distribution. This asymmetry does not appear in the simulation without radiation. An explanation for such behavior can be attributed to the increase of the velocity field produced my the inclusion of radiative effects. Indeed, a simple inspection of Fig. 10 reveals that the radiative source has increased the buoyancy force which turns to a faster advection of the flame front. Taking into account this increase in the velocity field along with the considered Reynolds
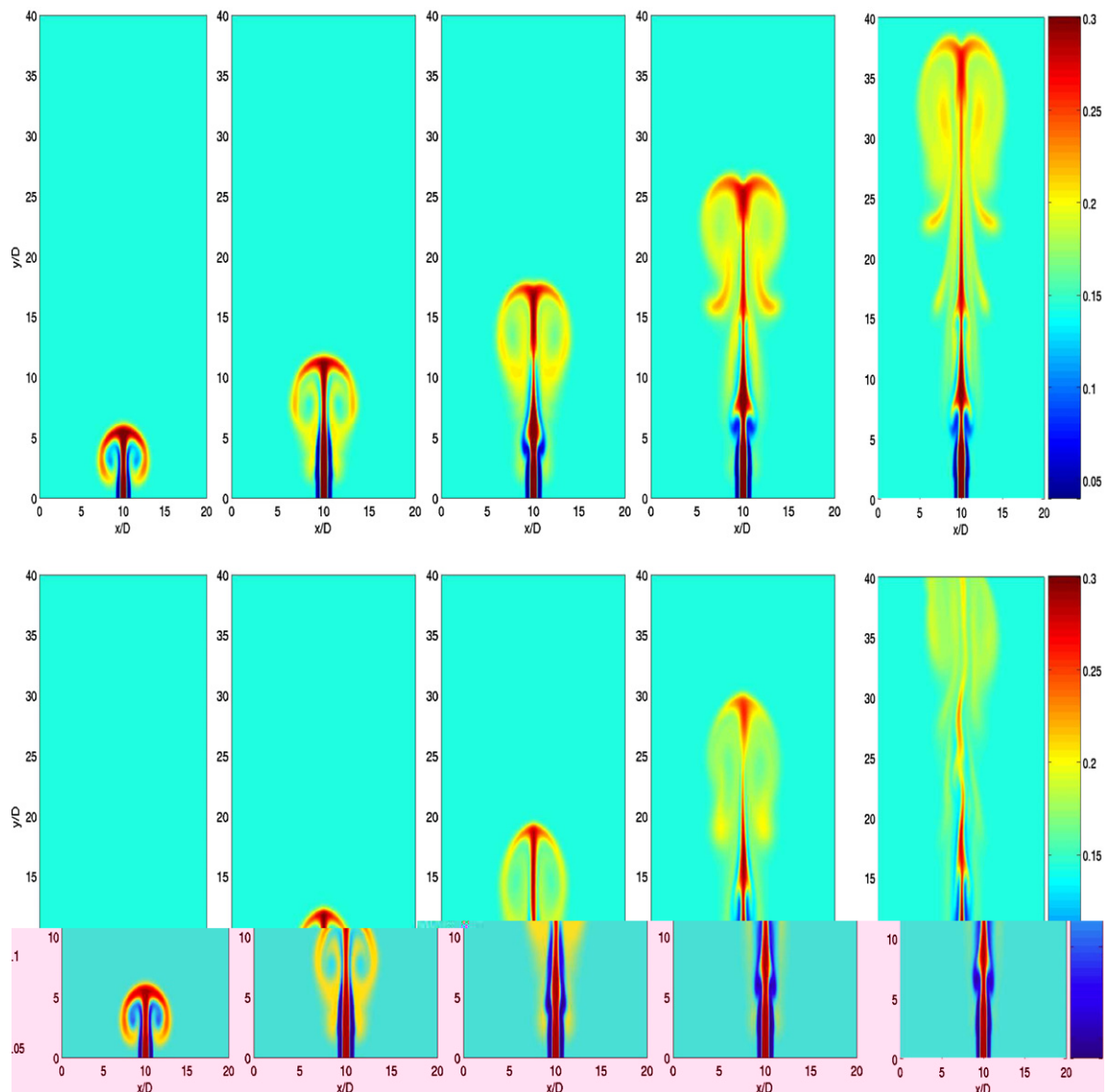

Fig. 11. Evolution of CO_2 mass fraction without radiation (upper row) and with M_1 model (lower row) at times (from left to right) $t = 0.002$, $t = 0.004$, $t = 0.006$, $t = 0.009$ and $t = 0.013$ s.

number, the flow appeared to change from laminar to turbulent regime. Hence, the asymmetric behavior is a consequence of turbulent effects.

To value the role of radiation on the participating gas, we display in Figs. 11 and 12 the distribution of mass fractions of the two selected species H_2O and CO_2, respectively. Examination of other species in the flame reveals similar trends. Note that, the flame stretching plays an important role in the production of CO_2 in the high scalar dissipation rate range, namely, the stronger the stretching, the more incomplete the reactions and the higher the CO_2 concentration. It is clear that accounting for radiation in the simulations, by M_1 model, can affect not only the flame temperature but also concentrations of species such as H_2O and CO_2. For the considered flame conditions, concentration of H_2O displays maximum values in the annular regions where the flame temperatures are also very high. The M_1 model affects the computed CO_2 mass fraction at all simulation times. These results offer a comprehensive study of the effects of thermal radiation on the overall
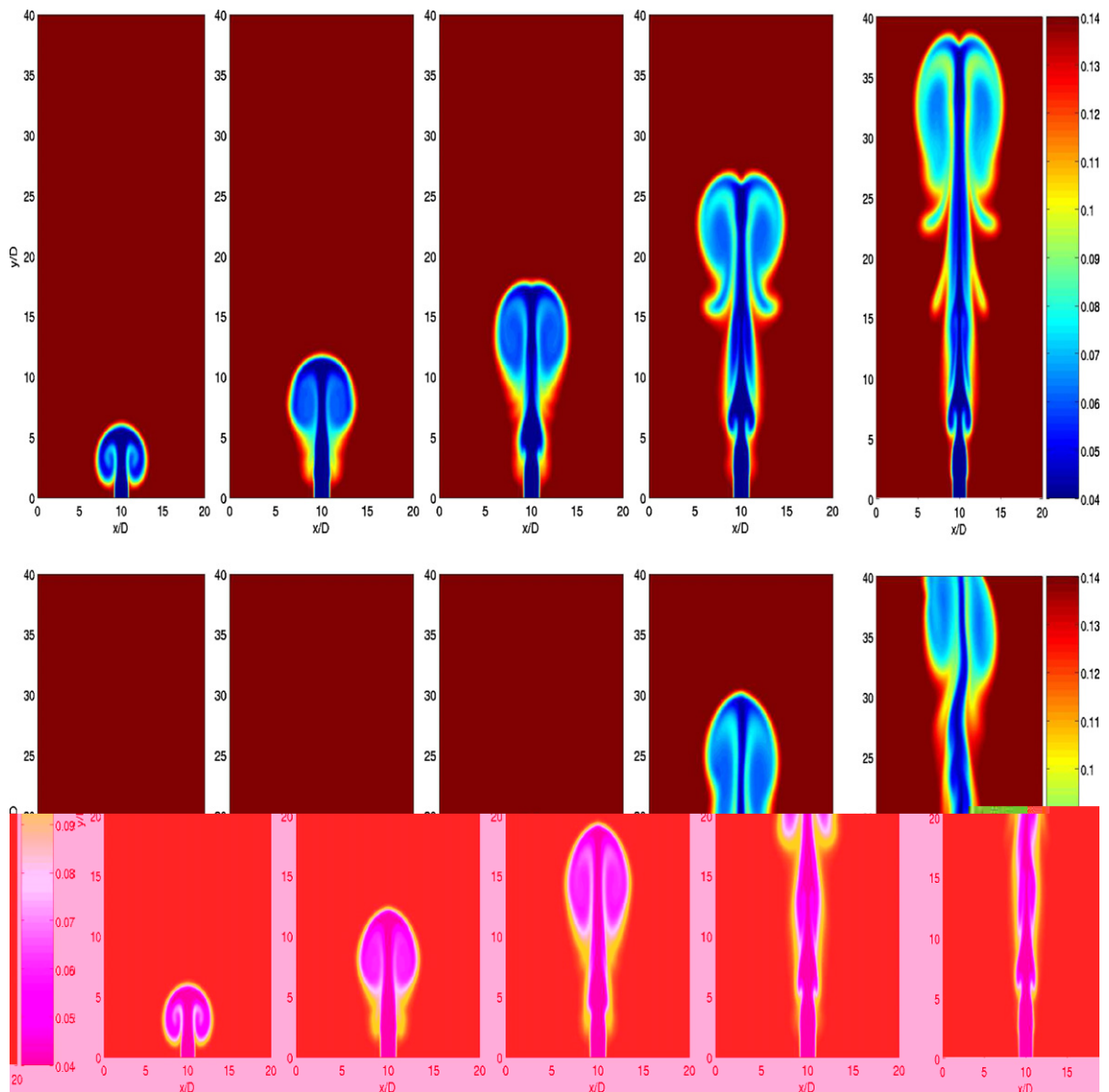

Fig. 12. Evolution of H_2O mass fraction without radiation (upper row) and with M_1 model (lower row) at times (from left to right) $t = 0.002$, $t = 0.004$, $t = 0.006$, $t = 0.009$ and $t = 0.013$ s.

flame modeling, since radiation heat transfer, energy conservation, and combustion chemistry are fully coupled in any combustion system or flame problem.

More comparisons are displayed in Figs. 13 and 14 by plotting cross-sections at the axial location $x = 10D$ for temperature, velocity, CO_2 and H_2O mass fractions. The temperature and the v-velocity profiles in Fig. 13 clearly show the difference of their behaviors when radiation and no-radiation computations are carried out. The radiation from the participating gas decreases the maximum value of the gas temperature near the flame. For our flame conditions, the M_1-model also decreases the v-velocity along the axial direction in the flame.
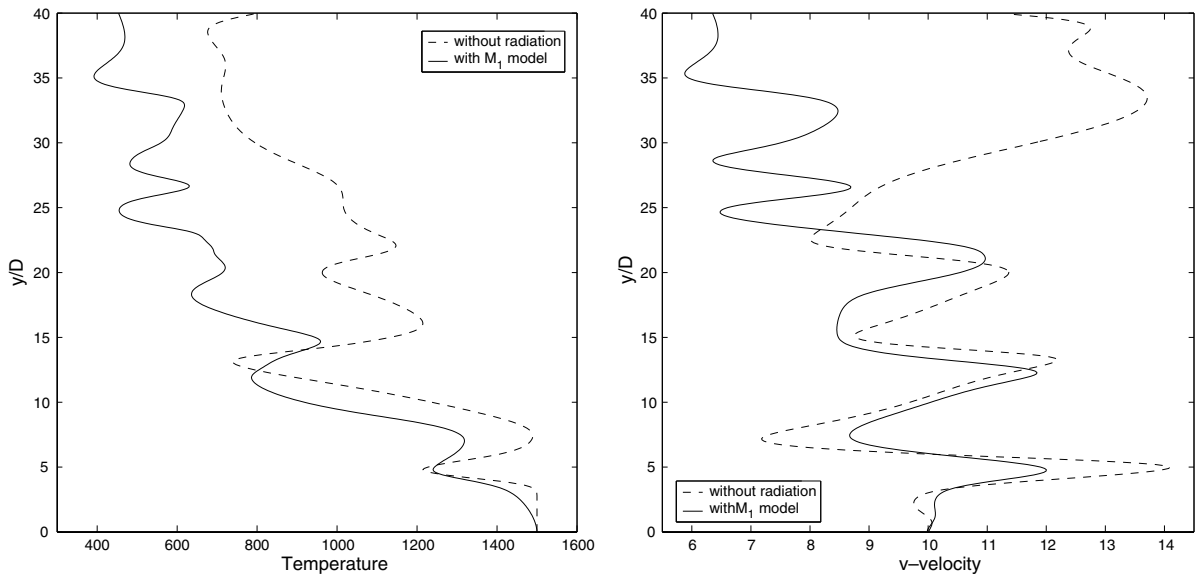

Fig. 13. Cross-section at mid-plane of $x = 10D$ of the temperature (left) and v-velocity (right).
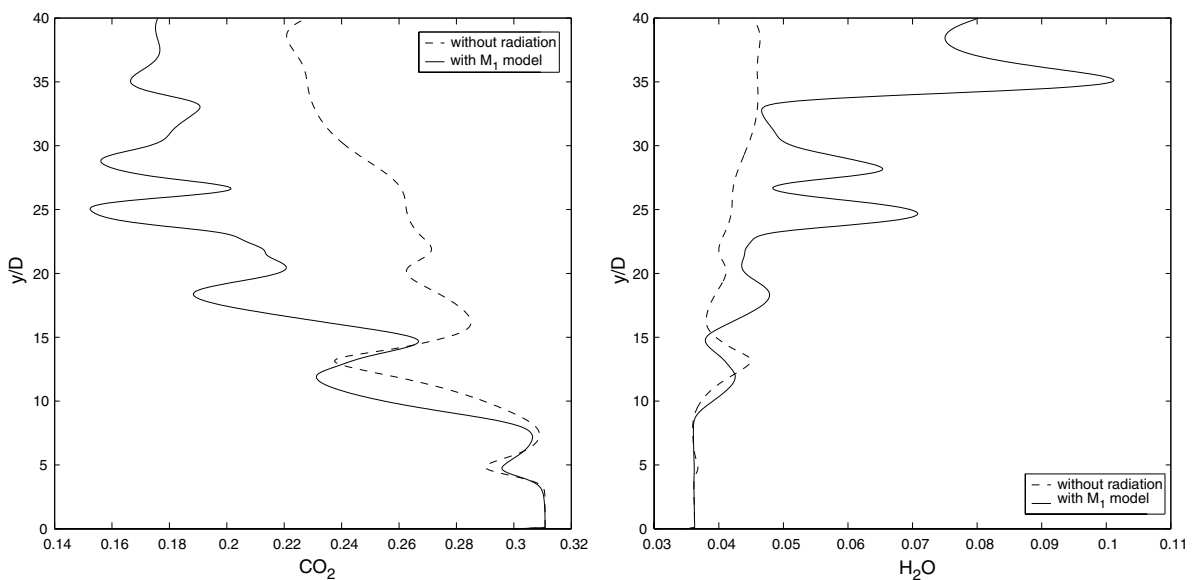

Fig. 14. Cross-section at mid-plane of $x = 10D$ of the CO_2 species (left) and H_2O species (right).

The calculated CO_2 and H_2O mass fractions shown in Fig. 14, indicate that the CO_2 species substantially decreases in the M_1 model. However, the H_2O mass fraction increases in the M_1-radiation calculation. As might be expected, a lower peak CO_2 mass fraction is associated with a lower local flame temperature. Here, the M_1-radiation calculation yields a peak CO_2 mass fraction that is 30.97% lower than that from the no-radiation calculation.

Finally it is worth pointing out that the additional CPU time required to carry out a step with the M_1-radiation model is about 21.81% costly than a computational step in no-radiation simulation. According to these computational costs and the accuracy obtained, the M_1 model can be considered more appropriate than the discrete-ordinate models, widely used in computational radiative transfer, to perform numerical studies on reacting radiating flows, in terms of both numerical credibility and computational cost. This is an important result when it comes to simplified heat transfer analysis in combustion simulations, given that the M_1 model is significantly simpler than the discrete-ordinate radiative transfer, regarding mathematics and implementation effort. It is important to note that the M_1 model offers a significant convenience for practical applications, that it can easily be incorporated in any existing CFD code by simply introducing a couple of hyperbolic partial differential equations into the calculations, describing the radiative energy and the radiative flux.

5. Conclusions

This work contributes to the investigation of consistent radiative models for the coupling of radiation and hydrodynamics at low-Mach numbers. Focusing on the moment method for radiative transfer, we analyzed the impact of radiation in chemically reacting flows at low Mach number. Starting from the full compressible Navier–Stokes equations and applying a low-Mach asymptotic, we have reconstructed a flow model able to remove the compressibility effects but preserves density variation. A simplified four-step chemical reactions are used for reacting species. Using the entropy M_1 method in radiation transport, the radiative transfer equation is transformed to a hyperbolic system independent of angular variables and easy to implement in an existing solver for reacting flows. A modified projection method for the flow equations has been combined with an HLL-type scheme for radiation transport. The resulted numerical method uses a staggered grid arrangement in space. The upwind differencing for convection terms, the central differencing terms and the averaging on the staggered grid stabilize the algorithm in the vicinity of discontinuities.

We have first compared results obtained using the M_1 model to those obtained using a direct kinetic solver for a two-dimensional test example on purely static radiative transfer. The agreement between the two results is good, showing that the radiative energy is accurately reproduced with the M_1 model at very low computational cost compared to the direct kinetic solver. Next we have considered the test example of non-reacting natural convection with large temperature difference in a squared enclosure. It has been shown that both, temperature distribution and velocity field are affected by the presence of radiation in the enclosure. The presented results indicate that the M_1 model can serve as efficient solver to be integrated into existing software packages for natural convection. In a third step we have investigated a diffusion methane/air flame with consideration of the radiation effects in a non-gray participating media. The evolution of temperature, velocity and species show large differences when computations are carried out with or without radiation effects. We have shown again that the flame behavior is very well described by the low-Mach and M_1 equations. It has been observed that the M_1 model can be considered as fast procedure for solving radiation effects in diffusion flames with a good accuracy. In addition, the M_1 model is an hyperbolic system of partial differential equations providing convenience in discretization of the transport equations in flow and combustion.

Since second order methods are widely used in CFD codes for practical applications, the coupling between the M_1 model and the low-Mach equations will be further investigated in the future. Other future works include the incorporation of turbulent effects in fluid dynamics equations, soot formation in radiative transfer, and also implementation of the models for reacting flow problems in three space dimensions.

Acknowledgments

Part of this work was carried out during a visiting stay of M. Seaïd at Department of Mathématiques Appliquées de Bordeaux. The authors acknowledge the funding by the Deutsche ForschungsGemeinschaft in the collaborative research center SFB568 "Flow and Combustion in Future Gas Turbine Combustion Chambers" at the University of Darmstadt.

References

[1] A.M. Anile, S. Pennisi, M.A. Sammartino, A thermodynamical approach to Eddington factors, J. Math. Phys. 32 (1991) 544–550.
[2] E. Audit, P. Charrier, J.P. Chize, B. Dubroca, A radiation-hydrodynamics scheme valid from the transport to the diffusion limit, 2002. Available from lanl.arxiv.org/abs/astro-ph/0206281.
[3] B. Dubroca, A. Klar, Half moment closure for radiative transfer equations, J. Comput. Phys. 180 (2002) 1–13.
[4] B. Dubroca, J.L. Feugeas, Entropy moment closure hierarchy for the radiative transfer equation, C. R. Acd. Paris, Sér. I, Math. 329 (1999) 915–920.
[5] W. Fiveland, The selection of discrete ordinate quadrature sets for anisotropic scattering, ASME HTD. Fundam. Radiat. Heat Transfer 160 (1991) 89–96.
[6] M. Frank, M. Seaïd, J. Janicka, A. Klar, R. Pinnau, G. Thömmes, A comparison of approximate models for radiation in gas turbines, Int. J. Prog. CFD 3 (2004) 191–197.
[7] I. Gasser, J. Struckmeier, I. Teleaga, Modelling and simulation of fires in vehicle tunnels, Int. J. Numer. Methods Fluids 44 (2004) 277–296.
[9] A. Harten, P.D. Lax, B. Van Leer, On upstreaming differencing and Godunov-type schemes for hyperbolic conservation laws, SIAM Rev. 25 (1983) 35.
[10] R.J. Kee, F.M. Rupley, E. Meeks, J.A. Miller, Chemkin-III: A Fortran chemical kinetics package for the analysis of gas phase chemical and plasma kinetics, Sandia Laboratories, SAND96-8216, 1996.
[11] S. Klainerman, A.J. Majda, Compressible and incompressible fluids, Commun. Pure Appl. Math. 35 (1982) 629–651.
[12] E. Larsen, G. Thömmes, A. Klar, M. Seaïd, T. Götz, Simplified P_N approximations to the equations of radiative heat transfer and applications, J. Comput. Phys. 183 (2002) 652–675.
[13] G. Lauriat, Combined radiation–convection in gray fluids enclosed in vertical cavities, J. Heat Transfer 104 (1982) 609–615.
[14] C.D. Levermore, Relating Eddington factors to flux limiters, J. Quant. Spectrosc. Radiat. Transfer 31 (1984) 149–160.
[15] P. LeQuéré, C. Weisman, H. Paillére, J. Vierendeels, E. Dick, R. Becker, M. Braack, J. Locke, Modelling of natural convection flows with large temperature differences: a benchmark problem for low mach number solvers, ESIAM: M2AN 39 (2005) 609–616.
[16] F. Liu, H. Becker, Y. Bindar, A comparative study of radiative heat transfer modelling in gas-fired furnaces using the simple grey gas and the weighted-sum-of grey-gases models, Int. J. Heat Mass Transfer 41 (1998) 3357–3371.
[17] M. Majda, J. Sethian, The derivation and numerical solution of the equations for zero Mach number combustion, Combust. Sci. Technol. 42 (1985) 185–205.
[18] D. Mihalas, B.S. Mihalas, Foundations of Radiation Hydrodynamics, Oxford University Press, New York, 1983.
[19] M.F. Modest, Radiative Heat Transfer, McGraw-Hill, New York, 1993.
[20] C. Pantano, Direct simulation of methane–air flame extinction, J. Fluid Mech. 514 (2004) 231–270.
[21] R.B. Pember, A.S. Almgren, J.B. Bell, P. Colella, L. Howell, M. Lai, A higher-order projection method for the simulation of unsteady turbulent nonpremixed combustion in an industrial burner, in: Proceedings of the 8th International Symposium on Transport Phenomena in Combustion, San Francisco, CA, 1995, pp. 16–20.
[22] G.C. Pomraning, The Equations of Radiation Hydrodynamics, Science Applications, 1973.
[23] J.F. Ripoll, B. Dubroca, G. Duffa, Modelling radiative mean absorption coefficients, Combust. Theory Modelling 5 (2001) 261–275.
[24] J.F. Ripoll, B. Dubroca, E. Audit, A factored operator method for solving coupled radiation-hydrodynamics models, Transp. Theory Stat. Phys. 31 (2002) 531–557.
[25] P.L. Roe, Approximate Riemann solvers, parameter vectors, and difference schemes, J. Comput. Phys. 43 (1981) 357–372.
[27] M.D. Smooke, V. Giovangigli, Reduced Kinetic Mechanisms and Asymptotic Approximations for Methane–Air Flames, Springer, Berlin, 1991, pp. 1–28, Chapter 1.
[28] M. Seaïd, M. Frank, A. Klar, R. Pinnau, G. Thömmes, Efficient numerical methods for radiation in gas turbines, J. Comput. Appl. Math. 170 (2004) 217–239.
[29] M. Seaïd, B. Dubroca, A. Klar, Flux limiters in the coupling of radiation and hydrodynamics models, J. Comput. Appl. Math. 168 (2004) 425–435.
[30] M. Seaïd, A. Klar, Efficient preconditioning of linear systems arising from the discretization of radiative transfer equation, Lect. Notes Comput. Sci. Eng. 35 (2003) 211–236.
[31] K. Seshadi, N. Peters, Asymptotic structure and extinction of methane–air diffusion flames, Combust. Flame 73 (1988) 23–44.
[32] I. Teleaga, Explicit representation of the static pressure in case of low-Mach approximation (submitted).
[33] I. Teleaga, M. Seaïd, I. Gasser, A. Klar, J. Struckmeier, Radiation models for thermal flows at low Mach number, J. Comput. Phys. 215 (2006) 506–525.

[35] R. Turpault, A consistent multigroup model for radiative transfer and its underlying mean opacities, J. Quant. Spect. Radiat. Transfer. 94 (2005) 357–371.
[37] J. Warnatz, in: W.C. Gardiner (Ed.), Combustion Chemistry, Springer, Berlin, 1984, pp. 197–360.
[38] J. Welch, F.H. Harlow, J.P. Shannon, B.J. Daly The MAC method a computing technique for solving viscous, incompressible, transient fluid-flow problems involving free surfaces, Los Alamos Scientific Laboratory, California, LA-3425, 1966.
[39] F.A. Williams, Combustion Theory, Cummings Publ. Co, 1985.